Machine Learning Assisted Chemical Characterization and Optical Properties of Atmospheric Brown Carbon in Nanjing, China

Yu Huang[1], Xingru Li[2], Dan Dan Huang[3], Ruoyuan Lei[1], Binhuang Zhou[1], Yunjiang Zhang[1], Xinlei Ge[1, 4]*

[1] Jiangsu Key Laboratory of Atmospheric Environment Monitoring and Pollution Control, Collaborative Innovation Center of Atmospheric Environment and Equipment Technology, School of Environmental Science and Engineering, Nanjing University of Information Science and Technology, Nanjing 210044, China

[2] Analytical Instrumentation Center, Department of Chemistry, Capital Normal University, Beijing, 100048, China

[3] Shanghai Academy of Environmental Sciences, Shanghai 200233, China

[4] School of Environment and Energy Engineering, Anhui Jianzhu University, Hefei 230601, China

*Corresponding author: Xinlei Ge (Email: caxinra@163.com)

For *Atmospheric Chemistry and Physics*

Abstract: The light-absorbing organics, namely brown carbon (BrC), can significantly affect atmospheric visibility and radiative forcing, yet current knowledge of chemical composition of BrC is largely limited to a number of certain classes of compounds; the chemical and optical properties, and particularly linkage between the two remain poorly understood. To address this, a comprehensive analysis was conducted on the particulate matter ($PM_{2.5}$) samples collected in Nanjing, China during 2022 ~ 2023 with a focus on the identification of key BrC molecules. Several important clues related to BrC were found. First, the water-soluble organic aerosol (WSOA) was more oxygenated during cold season (CS) due to a highly oxidized secondary OA (SOA) factor that was strongly associated with aqueous/heterogeneous reactions especially during nighttime, while the WSOA during summer season (SS) was less oxygenated and the SOA was mainly from photochemical reactions. Fossil fuel combustion hydrocarbon-like OA was the largest and dominant contributor to the light absorption during CS (55.6 ~ 63.7%). Secondly, our observations reveals that aqueous oxidation can lead to notable photo-enhancement during CS, while photochemical oxidation on the contrary caused photo-bleaching during SS; Both water-soluble and methanol-soluble organics had four key fluorophores, including three factors relevant with humic-like substances (HULIS) and one protein-like component. Thirdly, molecular characterization show that CHON compounds were overall the most abundant species, followed by CHO and CHN compounds, and significant presence of organosulfates in CS samples reaffirmed the importance of aqueous-phase formation. Finally, building upon the molecular characterization and light absorption measurement results, the machine learning approach was applied to identify the key BrC molecules, and 31 compounds including polycyclic aromatic hydrocarbons (PAHs), oxyheterocyclic PAHs, quinones, and nitrogen-containing species, etc., which can be a good reference for future studies.

1 Introduction

In ambient air, some organic aerosol (OA) species can absorb light in the near-ultraviolet (UV) and visible spectrum, termed as "brown carbon (BrC)" (Andreae and Gelencsér, 2006; Chen et al., 2020b). The BrC absorption exhibits strong wavelength-dependence that typically the absorption increases as the wavelength decreases (Laskin et al., 2015); it can also contribute to the darkening of ice and snow surfaces, particularly in low-latitude and polar regions (Yan et al., 2018; Brown et al., 2022; Chakrabarty et al., 2023). Thus, BrC can play a crucial role in global climate and air quality (Jo et al., 2016; Feng et al., 2013). Some studies show that the global radiative forcing of BrC ranges from approximately 0.22 to 0.57 W m^{-2}, equivalent to 27 ~ 70 % of that of black carbon (BC) (Lin et al., 2014; Zhang et al., 2017). Xu et al. (2024) used a global climate model to estimate that BrC accounts for 19% and 12% of the total light absorption by carbonaceous aerosols, with the direct radiative forcing of 0.110 W m^{-2} and 0.205 W m^{-2} in China during winter and summer, respectively. Delessio et al. (2024) estimated a top-of-the-atmosphere (TOA) radiative effect of BrC to be 0.04 W m^{-2}.

The sources of atmospheric BrC are highly complex, as it can originate from multiple primary sources (Hecobian et al., 2010; Chakrabarty et al., 2010; Gu et al., 2022) as well as various secondary chemical processes (Fleming et al., 2020; Jiang et al., 2021; Chen et al., 2020b; Wang et al., 2021) (Fleming et al., 2020; Jiang et al., 2021; Chen et al., 2020b).. The primary sources mainly include coal combustion, biomass burning, and vehicular emissions (Wang et al., 2016; Sun et al., 2016; Qi et al., 2019; Chen et al., 2018; Gu et al., 2022); besides, a significant presence of chromophores originating from the ocean has been observed, indicating that the ocean/marine emission is likely also an important source of BrC (Cavalli et al., 2004). As said, secondary BrC species can be generated from many processes, for instances, the aromatic secondary OA (SOA) species formed under high NO$_x$ concentrations (Jaoui et al., 2006), reaction products of biogenic or anthropogenic SOAs with nitrogen-containing substances such as NH$_3$ and NH$_4^+$ (Liu et al., 2024), reaction products of biogenic or anthropogenic SOAs with nitrogen-containing substances such as NH$_3$ and

74   NH$_4^+$ (Updyke et al., 2012; Shapiro et al., 2009; Bones et al., 2010), and aqueous-phase

75   reaction products from various carbonyl/phenolic precursors in cloud, fog, and aerosol

76   water (Hu et al., 2017; Wang et al., 2021; Li et al., 2023; Ou et al., 2021).

77   The optical properties of BrC are closely related with sources and composition of

78   OA. Recent studies have linked BrC light absorption with various sources resolved

79   from factor analysis of OA determined by the aerosol mass spectrometry (AMS) (Chen

80   et al., 2020b; Zhong et al., 2023; Chen et al., 2016), and provided the mass absorption

81   efficiency (MAE) of individual BrC source/factor. Current studies have identified

82   several classes of light-absorbing organics in ambient OA, such as aromatic carboxylic

83   acids, phenols, nitroaromatic compounds (NACs), polycyclic aromatic hydrocarbons

84   (PAHs) and their derivatives (Lin et al., 2018; Huang et al., 2018; Wang et al., 2021;

85   Xing et al., 2023; Gu et al., 2022; Chen et al., 2020b; Kuang et al., 2023; Laskin et al.,

86   2025). Some lignin pyrolysis/burning products including coumarins, flavonoids,

87   stilbenes, and several sulfur-containing species are also significant BrC constituents

88   (Fleming et al., 2020; Budisulistiorini et al., 2017; Huang et al., 2022). Xing et al. (2023)

89   identified a series of BrC chromophores, encompassing nitrophenols, benzoic acids,

90   oxygenated PAHs, phenols, aryl amides/amines, phenylpropene derivatives, coumarins

91   and flavonoids, pyridines, and nitrobenzoic acids. Nevertheless, knowledge regarding

92   the molecular composition of BrC so far is still incomplete and the identified species

93   only occupy a limited fraction of the BrC total light absorption (<25%) (Wang et al.,

94   2024). For examples, Zhang et al. (2013) measured eight NACs in Los Angeles and

95   found that they contributed about 4 % of water-soluble BrC light absorption at 365 nm;

96   Huang et al. (2018) measured 18 PAHs and their derivatives in Xi'an and found that

97   they accounted for on average $\sim$ 1.7 % of the overall absorption of methanol-soluble

98   BrC; Gu et al. (2022) quantified eight NACs present in PM$_{2.5}$ during winter in Nanjing,

99   which together accounted for at most ~9 % of the total BrC absorption at 365 nm. On

100   the other hand, the fluorescent properties of OA can be determined by the excitation-

101   emission matrix (EEM) fluorescence spectroscopy (Murphy et al., 2013; Stubbins et al.,

102   2014). By performing the parallel factor analysis (PARAFAC) on EEM data, the key

103   fluorophores can be identified (Xie et al., 2020; Chen et al., 2020a; Chen et al., 2021).

104   These fluorophores are also linked with different sources such as biomass burning, coal

105   combustion, and vehicle emissions (Tang et al., 2020).

106   Emerging non-targeted approaches based on gas chromatography (GC) or liquid

107   chromatography (LC) coupled with high-resolution mass spectrometry can detect

108   hundreds to thousands of molecules in OA (Kuang et al., 2023; Mao et al., 2022),

109   enabling the identification of potential BrC species by connecting them with light

110   absorption of OA. However, these approaches often output multi-dimensional data with

111   numerous variables, which must be evaluated appropriately. Traditional statistical

112   methods often perform poorly when handling large datasets and fail to accurately

113   elucidate complex interplays among variables (Fasola et al., 2020). Machine learning

114   (ML) is a powerful tool to effectively resolve such nonlinear relationships and address

115   issues of collinearity among variables (Tang et al., 2024). For instances, Zhang et al.

116   (2023) employed the Random Forest (RF) algorithm to quantify the factors driving

117    $PM_{2.5}$ trends in Tibetan Plateau from 2015 to 2022, revealing the importance of

118   anthropogenic emission reductions, and a similar ML approach was used for resolving

119   the driving factors of ozone pollution too (Zhu et al., 2024). Li et al. (2022b) applied

120   the ML-RF approach to analyze the sources of OA in submicron PM (PM_1) and $PM_{2.5}$,

121   showing the importance of secondary processes in supermicron PM. Wang et al. (2022a)

122   integrated the positive matrix factorization (PMF) with a multi-layer perceptron (MLP)

123   neural network to analyze the sources of BrC light absorption. Very recently, Wang et

124   al. (2024) applied the ML method to predict the optical properties of BrC with known

125   chromophores.

126   In this study, we conducted a systematic investigation on the chemical and optical

127   properties on the fine particular matter ($PM_{2.5}$) samples in both daytime and nighttime

128   collected in Nanjing, China during summer and cold seasons of 2022 ~ 2023.

129   Particularly, for the first time, we applied the ML-RF algorithm to connect the light-

130   absorbing characteristics with the determined organic molecules, aiming to identify

131   more unknown key BrC molecules. Our findings regarding the BrC properties,

132 especially the BrC molecules identified can be a good reference, and the ML application

133 can be an example of practice for future studies as well.

134

135 **2 Experimental methods**

136 **2.1 Sampling site and sample collection**

137 The $PM_{2.5}$ filter samples were collected in Nanjing, China, from July 11 to August

138 23, 2022, November 30 to December 10, 2022, February 13 to February 20, 2023, and

139 March 3 to March 31, 2023. The first period represents the hot summer season (SS) (81

140 samples), and the later three periods represent the cold season (CS)(83 samples); note

141 samples were not collected during precipitation in both seasons. The sampling site was

142 located inside the campus of Nanjing University of Information Science and

143 Technology (32°12'20.82"N, 118°42'25.46"E). The site was in a suburban area,

144 surrounded by residential buildings, close to traffic arteries, and industrial zones

145 (including chemical engineering, petrochemical, power plants and ironmaking and

146 steelmaking plants).

147 A high volume sampler (Jinshida Ltd. Qingdao, China, model KB-1000) with a

148 flow rate of 1.05 m^3 min^{-1} was employed. $PM_{2.5}$ samples were collected on the prebaked

149 (450 ºC) quartz fiber filters (Pallflex, USA, size of 8 × 10 inch). Daytime samples were

150 collected from 08:00 to 18:00 (Local Beijing time), and nighttime samples were

151 collected from 19:00 to 07:00 on the next day. Each filter was wrapped in an aluminum

152 foil and kept frozen at -20 °C until analysis. The concentrations of common gas

153 pollutants (SO_2, NO_2, CO, and O_3) were obtained from the nearby National

154 Environmental Monitoring Center (http://www.cnemc.cn/), while the meteorological

155 parameters (air temperature, relative humidity, wind speed and direction) were recorded

156 in the same site as $PM_{2.5}$.

157

2.2 Chemical analyses

2.2.1 Measurements of inorganic ions, organic carbon (OC) and elemental carbon (EC)

A number of round pieces (20 mm diameter) were punched from each sample filter, and were extracted by using 50 mL of ultrapure water (18.25 MΩ cm) (10 pieces) and methanol (4 pieces), respectively. The filter pieces underwent 30 minutes of sonication and were filtrated through the polytetrafluoroethylene (PTFE) syringe filters (0.22 μm) to remove insoluble materials. Cations (NH_4^+, Na^+, K^+, Mg^{2+}, Ca^{2+}) were measured using a 881 Compact IC Pro (Metrohm, Switzerland), anions (NO_3^-, SO_4^{2-}, Cl^-, F^-) were determined by the ICS2100 (Dionex, USA). The water-soluble organic carbon (WSOC) (μg C m^{-3}) was measured by a total organic carbon (TOC) analyzer (TOC-L, Shimazu, Japan). Operational details of these analyses can be found in our previous work (Chen et al., 2020a).

Concentrations of total elemental carbon (EC) and organic carbon (OC) in samples were measured using a thermal optical carbon analyzer (RT-4; Sunset Laboratory, USA) on a separate round filter piece (17 mm diameter) by using the IMPROVE TOT protocol (Bai et al., 2020). In addition, the residual OC and EC contents in samples after methanol extraction were determined with the same method above, and were subtracted from the total OC content, to derive the methanol-soluble OC (MSOC) (μg C m^{-3}).

2.2.2 Bulk analysis of organics

We employed specially an Aerodyne soot particle AMS (SP-AMS) to determine the bulk composition of water-soluble OA (WSOA) (Onasch et al., 2012). It should be noted that, direct AMS analysis on the methanol-soluble OA (MSOA) is currently unfeasible, even though it might be more important than WSOA in both concentration and light absorption. Likewise almost all offline AMS analysis methods (O'brien et al., 2019; Vasilakopoulou et al., 2023), this is due to that the methanol solvent and its associated organic impurities cannot be effectively removed, making the obtained MSOA signals unidentifiable.

The analysis procedure of WSOA is similar to that described in Ge et al. (2017). In

187   brief, eight round pieces (20 mm diameter) of each filter were sonicated in 40 mL of

188   ultrapure water, and the aqueous extract was nebulized using an atomizer (TSI, Model

189   3076), then the mist was dried by a silica gel diffusion dryer and the remaining particles

190   were sent to the SP-AMS. The SP-AMS was operated in a laser-off mode, therefore it

191   measured non-refractory species that can be rapidly vaporized at 600 °C (SP-AMS oven

192   temperature). Note the SP-AMS employs a 70 eV electron impact (EI) ionization

193   scheme, so the vaporized species are fragmented into positively charged ions with

194   different mass-to-charge (m/z) ratios and we obtained the composition of WSOA in the

195   form of lumped molecular fragments rather than detailed molecular composition.

196   The SP-AMS data were post-processed using the Igor-based ToF-AMS analysis

197   toolkit (SQUIRREL version 1.56D and PIKA version 1.15D). Elemental ratios

198   including hydrogen-to-carbon (H/C), oxygen-to-carbon (O/C) and nitrogen-to-carbon

199   (N/C) as well as the organic mass to organic carbon (OM/OC) ratio were calculated by

200   using the methods proposed in Aiken et al. (2008), Canagaratna et al. (2015) and Ge et

201   al. (2024). The WSOA mass concentration of each sample was normalized by

202   multiplying the WSOC concentration with its corresponding OM/OC. Then, we

203   conducted the PMF analysis to resolve the sources of WSOA by utilizing the PMF

204   evaluation toolkit (Version 2.06) (Ulbrich et al., 2009), followed strictly the protocol

205   described in Zhang et al. (2011). As usual, we included only ions with $m/z \leq 120$, and

206   PMF solutions were explored by varying the number of factors (from 3 to 8) and

207   rotation parameters (f_{peak}, from -1 to 1 with an increment of 0.2). Based on the

208   diagnostic plots in Fig. S1 in the supplement, the four-factor solution was selected as

209   the best solution. The factors include a hydrocarbon-like OA (HOA) relevant with fossil

210   fuel combustion, a biomass burning-related OA (BBOA), a less oxidized oxygenated

211   OA (OOA1) and a more oxidized oxygenated OA (OOA2) (see details in Sect. 3.1.2).

212   **2.2.3 Molecular characterization of organics**

213   Molecular-level characterization of organic species was conducted by using an

214   ultra-high performance liquid chromatography with a quadrupole time-of-flight (QTOF)

215   mass spectrometer (UPLC-QTOF-MS) (ACQUITY UPLC H-Class coupled with a

216 Xevo G2-XS QTOF, Waters). The sample pretreatment was described in Text S1, and

217 the analyzed organics are those dissolved in methanol (namely MSOA). Compound

218 separation was performed with a Luna Omega 1.6 μm C18 column (100 mm × 2.1 mm

219 × 1.6 μm), and the sample aliquot was subjected to electrospray ionization (ESI), and

220 detected in both positive and negative ion modes. The scanning m/z range for each mass

221 spectrum was 50-1200, with a scanning rate of one spectrum per 0.1 second. More

222 details are presented in Text S2.

223   The original UPLC-QTOF-MS data were processed using the Mass Spectrometry-

224 Data Independent Analysis (MS-DIAL, version 4.92) software (Tsugawa et al., 2015),

225 including peak extraction, alignment and deconvolution, achieving a detection

226 probability of 70% in all samples for any identified compound. The method of

227 systematic error removal using random forest (SERRF, a ML algorithm), was then

228 introduced to reduce systematic errors and normalize the measured data (Fig. S2). All

229 deconvoluted spectra were imported into the SIRIUS (Version 5.6.2) toolkit (Dührkop

230 et al., 2019) to determine molecular formulas. The semi-quantitative concentrations of

231 identified molecules were expressed in the normalized peak areas (NPRs), defined as

232 their peak areas acquired from SERRF divided by air volumes of the samples.

233   In addition, the double-bond equivalent (DBE) was used to indicate the level of

234 unsaturation of the compound (Bae et al., 2011), and the aromaticity equivalent (Xc)

235 (Yassine et al., 2014) was used to indicate the molecular structure. O/C, H/C and DBE

236 values of the sample were averaged over all identified molecules based on their relative

237 abundances (See details in Text S3).

238

239   **2.3 Optical analyses**

240   **2.3.1 Light absorption properties**

241   The light absorption spectra of both WSOC and MSOC in 200 ~ 800 nm were

242 obtained using a UV-Vis spectrophotometer (UV-3600, Shimadzu, Japan) with a 0.5 nm

243 interval. The absorbance at a certain wavelength λ ($A_λ$) were corrected by subtracting

244 that at 700 nm (A_{700}) (near zero, as background), and the corresponding light absorption

coefficient (Abs_λ, M m^{-1}) is calculated as below (Hecobian et al., 2010):

$$Abs_\lambda = (A_\lambda - A_{700}) \times \frac{V_l}{V_a \times L} \times \ln(10) \qquad (1)$$

Where V_l represents volume of the extract (water or methanol), V_a denotes air volume of the filter piece, and L is the optical path length (0.01 meters here).

The corresponding mass absorption efficiency (MAE_λ, m^2 g^{-1}) can then be calculated below:

$$MAE_\lambda = \frac{Abs_\lambda}{[WSOC] \ ([MSOC])} \qquad (2)$$

Where [WSOC] ([MSOC]) represents the mass concentration of WSOC (MSOC). Following previous studies (Laskin et al., 2015; Chen et al., 2018; Xie et al., 2020; Chen et al., 2020b), the light absorption at 365 nm (Abs_{365}) was employed as a surrogate for BrC in this work.

The relationship between the Absorption Ångström Exponent (AAE)(an index of the wavelength dependence) (Andreae and Gelencsér, 2006) and light absorption is shown below:

$$Abs_\lambda = K \cdot \lambda^{-AAE} \qquad (3)$$

Where K is a constant related to light absorption, and we computed the AAE values in the 300 ~ 450 nm range.

Additionally, a multi-linear regression (MLR) method was used to estimate the contributions of different WSOA factors to the light absorption of total WSOA, as shown in the following equation :

$$Abs_{365,WSOC} = a \times HOA + b \times BBOA + c \times OOA1 + d \times OOA2 \qquad (4)$$

Here, HOA, BBOA, OOA1, and OOA2 represent time series of the WSOA factors. a, b, c, and d are the fitting parameters, which are the mass absorption efficiency (MAE) values of corresponding factor.

The direct radiative forcing effect of BrC can be represented by the simple forcing efficiency (SFE) (in W g^{-1}), which is the energy added to the earth-atmosphere system per unit mass of aerosol (Bond and Bergstrom, 2006). The SFE of BrC at the wavelength λ can be expressed below (Chen and Bond, 2010):

273
$$\frac{dSFE}{d\lambda} = -\frac{1}{4}\frac{dS(\lambda)}{d\lambda}\tau_{atm}^2(\lambda)(1-F_C)$$
$$[2\times(1-\alpha_S)^2\beta(\lambda)MSE(\lambda)-4\times\alpha_S\times MAE(\lambda)]d\lambda \qquad (5)$$

274   Where $S(\lambda)$ represents the solar irradiance at λ obtained from the ASTM G173–03

275 reference spectra. τ_{atm} denotes the atmospheric transmission (0.79), F_C is set to 0.6,

276 indicating the fraction of cloud cover, the global average value of α_s is fixed at 0.19,

277 representing the surface albedo, β is the backscatter fraction, and MSE and MAE are

278 the mass scattering efficiency and mass absorption efficiency of BrC, respectively. .

279   When estimating the radiative effect of BrC, the direct radiative forcing caused by

280 aerosol scattering can be neglected. Therefore, the absorbed radiative forcing within a

281 given spectral range is calculated by the simplified Eq. (6):

282
$$SFE = \int \frac{dS(\lambda)}{d_\lambda}\tau_{atm}^2(\lambda)(1-F_C)\times\alpha_S\times MAE(\lambda)\,d\lambda \qquad (6)$$

283   **2.3.2 Fluorescence properties**

284   Characterization of excitation-emission matrix (EEM) of the extracts was

285 performed using a fluorescence spectrophotometer (Cary Eclipse, Agilent, USA) The

286 wavelength range of excitation was set from 230 to 500 nm, and that of emission was

287 from 250 to 600 nm, the scanning resolutions of excitation and emission were 5 nm and

288 2 nm, respectively, with the scanning speed of 1200 nm min^{-1}. The photomultiplier tube

289 (PMT) detector voltage was set at 600 V. The measurement was subjected to instrument

290 calibration, internal filter correction, Raman/Rayleigh scattering correction, and all

291 EEM spectra were subjected to blank filter subtraction. The processed data were further

292 analyzed using PARAFAC to group potential components with similar fluorescent

293 properties. The analysis was performed using MATLAB 2022b software with the

294 drEEM toolbox (Murphy et al., 2013).

295   Fluorescent properties of the extracts were also characterized by the humification

296 index (HIX), biological index (BIX), and fluorescence index (FI). HIX is defined as the

297 ratio of integrated fluorescence emission intensity in the range of 435 - 480 nm to that

298 in the range of 300 to 345 nm when excited at 254 nm; BIX is calculated as the ratio of

299 emission intensity at 380 nm to that of 430 nm for the excitation wavelength of 310 nm;

300 FI is the ratio of emission intensity at 470 nm to that of 520 nm under a fixed 370 nm

301   excitation wavelength (Birdwell and Engel, 2010; Mcknight et al., 2001).

302

303   **2.4 Machine learning identification of key light-absorbing species**

304   The ML RF model was used here to screen the key light absorbing species by

305   linking the target variable (Abs_{365}) with the identified organic molecules (in NPRs), via

306   the "randomforest()" function in R software (Version 4.3.2). Note ~~both~~since molecular

307   characterization was conducted on MSOA (not WSOA), therefore light absorption ~~and~~

308   ~~organic molecules are~~data of MSOA were also used here for ~~MSOA~~consistency. The

309   model included 500 decision trees and estimated the variance through a cross-validation

310   during training. The dataset was divided into a training set (80% of total) and a test set

311   (20% of total) to assure accuracy and robustness of the model.

312   The model outputted two key indices to assess the importance of each molecule to

313   the light absorption. One metric is IncNPu_val, which can measure the purity of nodes.

314   During the construction of each tree in the RF model, each split can increase the purity

315   of nodes, therefore if more frequently a variable is used in splitting, more contribution

316   it has to the increase of purity of nodes, then the variable is considered to be important.

317   IncMSE_val is another index based on the mean squared error (MSE). When we

318   permute a variable, increase in the projected error can serve as a measure of its

319   importance. If a variable with a significant impact on the predicted results is permuted,

320   the model's MSE would increase significantly, resulting in a high IncMSE_val value

321   (González et al., 2015). Under the 50th percentile of IncMSE_val, some variables had

322   zero or even negative contributions to IncMSE_val. Considering the definition of

323   IncMSE_val, such variables would have either no or negative influence on model fitting,

324   thus only the top 50 % of compounds were chosen. Afterwards, intersection of the two

325   indices were considered as potential BrC chromophores.

326   Moreover, a molecule typically requires a substantial uninterrupted conjugation on

327   its molecular backbone to effectively absorb visible light (Lin et al., 2018), therefore a

328   compound with the ratio of DBE to carbon (DBE/C) greater than that of linear polyenes

329   (with a molecular formula of C_xH_{x+2}, DBE/C = 0.5) (Cain et al., 2014) is treated as a

330   potential BrC compound. Besides, the DBE/C ratio should be less than the upper limit

331 of DBE for natural compounds (DBE/C = 0.9) (Lobodin et al., 2012). Finally, the

332 candidate compounds passed aforementioned criteria were compared with those in

333 open-source databases, including MoNA (https://mona.fiehnlab.ucdavis.edu/) and

334 MassBankEU (https://massbank.eu/), to be interpreted as the key BrC compounds.

335

336 **3 Results and discussion**

337 **3.1 Chemical properties**

338 **3.1.1 General characteristics**

339 During the sampling period, the temperatures were 34.34 ± 3.23 °C (daytime) (±

340 one standard deviation, hereinafter) and 30.85 ± 2.97 °C (nighttime) during SS, 13.00

341 ± 6.04 °C (daytime) and 9.97 ± 5.04 °C (nighttime) during CS, and the relative humidity

342 (RH) levels were 53.61 ± 10.33 % (daytime) and 65.88 ± 9.87 % (nighttime) during SS,

343 47.81 ± 18.94 % (daytime) and 55.56 ± 15.74 % (nighttime) during CS, respectively

344 (Figs. 1a and b). Figure 1c depicts the temporal variations of different components.

345 Average concentrations of OC, EC, WSOC, MSOC and total ionic species during

346 daytime and nighttime in the two seasons are summarized in Table 1. Clearly,

347 concentrations of all components were higher in CS than those in SS, but the

348 daytime/nighttime differences were relatively small in both seasons. Also, the MSOC

349 levels were larger than WSOC in all samples. MSOC occupied 82.4 % and 81.5 % while

350 WSOC occupied 61.3 % and 49.5 % of the total OC during SS and CS, respectively,

351 indicating that methanol can more effectively extract the aerosol organics than water.

352 The mean mass contributions of different ions to their total during SS and CS,

353 respectively are shown in Fig. 1c too. The particles were overall neutral as the molar

354 ratios of inorganic anions to cations were 0.97 and 0.98 during SS and CS, respectively

355 (Fig. S3). The most abundant ion was sulfate in SS (45.5 %) and nitrate in CS (50.7 %),

356 as low temperatures during CS favor the partitioning of nitrate to particle phase. As so,

357 the sulfur oxidation ratio (SOR, $[SO_4^{2-}]/([SO_4^{2-}]+[SO_2])$) and nitrogen oxidation ratio

358 (NOR, $[NO_3^-]/([NO_3^-]+[NO_2])$) were 0.58 and 0.16 (daytime) and 0.56, 0.17 (nighttime)

359 during SS, 0.40, 0.28 (daytime) and 0.42, 0.30 (nighttime) during CS, respectively.

360 NOR was indeed much higher in CS especially during nighttime than those in SS.

361 Furthermore, ammonium (NH_4^+) was the predominant cation while sulfate, nitrate and

362 chloride were major anions. The scatter plots of molar concentrations of ammonium

363 versus summed sulfate, nitrate and chloride (Fig. S4) reveal different bonding forms of

364 the aerosol inorganic salts in different seasons. The correlations were both tight

365 (correlation coefficients close to 1) yet the fitted slopes during SS were 0.80 (daytime)

366 and 0.89 (nighttime) while those during CS were 0.98 (daytime) and 0.99 (nighttime),

367 respectively. Such results demonstrate that ammonium was deficit to neutralize the

368 cations therefore significant amounts of metal salts (such as sodium/calcium

369 sulfate/nitrate) could exist during SS while during CS, most inorganic species were in

370 the forms of $(NH_4)_2SO_4$, NH_4NO_3 and NH_4Cl with no appreciable metal salts.

371 **3.1.2 Features and sources of water-soluble organics**

372 Regarding the water-soluble portion of organic species (WSOA), Figure 2a

373 presents the average high resolution mass spectra (HRMS) during SS and CS,

374 respectively. It can be seen that, WSOA during CS appeared to be much more

375 oxygenated than that during SS (O/C: 0.58, 0.59 vs. 0.44, 0.45) . To further unravel

376 causes of such differences, PMF analysis were conducted and the HRMS of resolved

377 factors are presented in Fig. 2b, while mass contributions of these factors during SS and

378 CS as well as the Pearson's correlation coefficents (*r*) of these factors with other

379 components are illustrated in Fig. 3.

380 The HOA MS was dominated by $C_xH_y^+$ ions (57.2 %), such as $C_4H_7^+$ (*m/z* 55) and

381 $C_4H_9^+$ (*m/z* 57), primarily originating from hydrocarbons emitted from fossil fuel

382 combustion (such as traffic) (Canagaratna et al., 2004). Among the four factors, HOA

383 exhibited the lowest O/C ratio (0.24) and the highest H/C ratio (1.66). This is consistent

384 with the behaviors of HOA from a number of previous offline AMS studies

385 (Daellenbach et al., 2017; Liu et al., 2021; Ye et al., 2017; Qiu et al., 2019). The second

386 factor was identified as BBOA, since it has distinct peaks at *m/z* 60 (mainly $C_2H_4O_2^+$,

387 0.76 % of the total HRMS) and *m/z* 73 (mainly $C_3H_5O_2^+$, 1.09 % of the total HRMS),

388 which are characteristic fragments associated with levoglucosan, a tracer compound of

389 biomass burning particles (Kumar et al., 2022; Qin et al., 2017). Correlations between

390 BBOA and these two tracer ions were indeed tight (0.71 with $C_2H_4O_2^+$ and 0.82 with

391 $C_3H_5O_2^+$). A notably positive correlation between BBOA and K^+ (Fig. 3b) further

392 supports its BB origin as K^+ is also a common BB emission tracer (Yu et al., 2018).

393 Note the BBOA here had a relatively higher O/C ratio of 0.61 than those identified in

394 previous offline AMS measurements, such as Yangzhou (0.45) (Ge et al., 2017), Beijing,

395 China (0.59) (Qiu et al., 2019), and Marseille, France (0.54) (Bozzetti et al., 2017),

396 suggesting the presence of partially aged BBOA species in this factor.

397   The other two factors are secondary. OOA1 was less oxidized with a O/C of 0.39

398 and OOA2 was more oxygenated with the highest O/C of 0.65 among all factors. OOA1

399 had characteristic fragments at m/z 29 (CHO^+) and m/z 43 (mainly $C_2H_3O^+$) while

400 OOA2 had the least fraction of oxygen-free $C_xH_y^+$ ions (28.5 %) but the largest fraction

401 of oxygenated ions (32.8 % of $C_xH_yO_1^+$ and 18.9 % of $C_xH_yO_2^+$) among the four factors.

402 OOA2 correlated well with CO_2^+ (m/z 44) (r of 0.81), a characterisitic ion of highly

403 oxygenated carboxylic/dicarboxylic acids. Moreover, OOA2 had the highest N/C of

404 0.095 as well as those of $C_xH_yN^+$ (9.1 %) (such as CH_2N^+, CHN^+ and CH_4N^+) and

405 $C_xH_yO_zN^+$ (3.8 %) (such as $CHON^+$, CH_2NO^+ and CH_4NO^+), indicating the presence of

406 amines and amino acids correspondingly (Ge et al., 2024). Besides, the N/C level of

407 OOA2 is close to that of fogwater observed in Fresno, indicating the aqueous phase

408 reactions are likely an source of those nitrogen-containing ions in OOA2 (Kim et al.,

409 2019). In addition, sulfur-containing organic ions (such as CH_2S^+, $CH_3SO_2^+$ and CHS^+)

410 were almost exclusively present in OOA2 and in a significant fraction (2.7 %), as such

411 ions were strongly associated with aqueous/heterogenous reactions (Zorn et al., 2008;

412 Huang et al., 2020; Petters et al., 2021; Mcneill, 2015), reassuring that OOA2 was very

413 likely linked with aqueous/heterogenous formation pathway.

414   The time series of mass contributions of the four factors are shown in Fig. 1d, and

415 significant differences can be observed during the two sampling seasons, as can be seen

416 clearly in Fig. 3a. HOA was a significant source in both SS and CS, and as expected, it

417 was higher during daytime due to the stronger traffic activities. BBOA was much less

418 important than HOA, but its contribution during CS was obviously more than that
419 during SS (12.5 ~ 13.0 % vs. 7.2 ~ 7.8 %), and accordingly, HOA contribution was
420 slightly larger during SS than during CS (38.0 ~ 41.7 % vs. 29.9 ~ 36.8 %). It is worthy
421 to mention that, BBOA can be more important than HOA, such as in Bejing during
422 autumn polluted period (38.3% of WSOA) (Hu et al., 2020) , in Delhi, India (31-34%
423 of WSOA) (Bhowmik et al., 2024), and in urban and rural Catalonia, Spain (up to 26%
424 of WSOA) (Veld et al., 2023). In general, the dominance of SOA in WSOA observed
425 here was consistent with most offline AMS studies aforementioned, except that POA was
426 found to dominate WSOA in Delhi, India (Bhowmik et al., 2024). However, mass
427 contributions of the two individual SOA factors in different seasons in this study were
428 strikingly different. OOA1 occupied nearly half of the total WSOA (47.5 ~ 49.8 %)
429 while contributions of OOA2 were only 3.0 ~ 5.0 % during SS; on the other hand,
430 OOA2 occupied 38.6 ~ 43.5 % of WSOA mass while those of OOA1 were down to
431 11.6 ~ 14.1 %. The much larger OOA2 fraction during CS explains its overall high
432 oxidation degree depicted in Fig. 2. These results are well consistent with our previous
433 studies, as we show that during summer in Nanjing, photochemical reactions dominate
434 the SOA formation and yield relatively less oxygenated OA (Xian et al., 2023; Wang et
435 al., 2022b), while during cold seasons, aqueous formation of SOA becomes more
436 important which can generate highly oxygenated OA (Wu et al., 2018). The air
437 temperature (a solar radiation indicator) and ozone (a photochemical product) both
438 correlated positively with OOA1 but negatively with OOA2 (Fig. 3b), further verifying
439 the dominance of photochemical production of OOA1 not OOA2. As is well known,
440 particulate nitrate was strongly associated with heterogenous reactions and gas-to-
441 particle partitioning favored by low temperature and high RH especailly during CS, and
442 indeed, OOA2 correlated much tighter with NH_4NO_3 than OOA1 did.
443
444 **3.2 Optical properties**
445 **3.2.1 Light-absorbing properties of WSOC and MSOC**
446 The average light absorption coefficients of BrC in WSOC and MSOC in 300 ~

447 700 nm during daytime and nighttime of SS and CS are illustrated in Fig. 4a. As

448 expected, the values all exponentially decreased as a function of wavelength. The

449 calculated AAE values are listed in Table 1. It is interesting to find that the WSOC AAE

450 had no significant difference between SS and CS (6.35 vs. 6.43), while that of MSOC

451 AAE appeared to be notable (5.99 vs. 6.89); Compared with the MSOC AAE, the

452 WSOC AAE was higher during SS but smaller during CS. The AAE values obtained

453 here are slightly smaller than those reported in Beijing (7.3 ~ 7.5 of WSOC) (Du et al.,

454 2014; Chen et al., 2016), comparable to that in Guangzhou (6.7 of WSOC) (Fan et al.,

455 2016). Note Chen and Bond (2010) reports that particles generated from smoldering of

456 various types of wood exhibit a AAE of 6.9 ~ 11.6 (MSOC); Lambe et al.(2013) shows

457 that lab-generated secondary BrC possesses a AAE of 5.2 ~ 8.8 (MSOC). Compared

458 with these values, our measured AAE values (<7) here probably suggest a dominance

459 of secondarily formed BrC for both WSOC and MSOC. This can be verified by Fig. 3a

460 for WSOC, as indeed it was dominated by SOA particularly during nighttime in both

461 seasons. However, the large difference in WSOA chemical composition in different

462 seasons (especially SOA proportions) did not result in a large difference in WSOC AAE,

463 demonstrating clearly the non-correspondence of chemical species to light-absorbing

464 species (a.k.a., BrC). On the contrary, for MSOC, the relatively large difference of

465 MSOC AAE in different seasons likely reflect the distinction of BrC species but not

466 necessarily chemical constitution. The light absorption coefficients at 365 nm (Abs_{365})

467 are listed in Table 1 too. The average $Abs_{365,\ WSOC}$ during CS (4.87 M m^{-1}) was

468 approximately 2.15 times that of SS (2.27 M m^{-1}), and that of MSOC during CS (4.97

469 M m^{-1}) was also much larger than that during SS (3.64 M m^{-1}); Nighttime values were

470 higher than those in daytime expect for WSOC during CS. For the same set of samples,

471 $Abs_{365,\ MSOC}$ values were typically larger than $Abs_{365,\ WSOC}$ except that CS daytime

472 $Abs_{365,\ MSOC}$ was slightly smaller than $Abs_{365,\ WSOC}$ (4.65 vs. 4.89 M m^{-1}). Scatter plots

473 of Abs_{365} versus WSOC (and MSOC), and $Abs_{365,\ WSOC}$ versus $Abs_{365,\ MSOC}$ for the four

474 series of samples are given in Fig. S5. The correlations were generally well especially

475 those of WSOC and MSOC ($r > 0.80$), suggesting that there is a large overlap of

476   extracted species between WSOC and MSOC, as well as their BrC constituents.

477   Regarding the MAE at 365 nm (MAE_{365}), $MAE_{365, WSOC}$ during CS (0.75 $m^2\ g^{-1}$)

478   was higher than that during SS (0.55 $m^2\ g^{-1}$), indicating its stronger light absorption

479   ability during CS; however, the $MAE_{365, MSOC}$, unlike $Abs_{365, MSOC}$, was smaller during

480   CS than that during SS (0.50 vs. 0.72 $m^2\ g^{-1}$). Besides, MAE_{365} values for both WSOC

481   and MSOC were slightly larger during nighttime than those during daytime in both

482   seasons. Compared to previous winter studies, the $MAE_{365, WSOC}$ in Nanjing here was

483   lower than that in Beijing (1.21 ~ 1.26 $m^2\ g^{-1}$) (Du et al., 2014; Chen et al., 2016; Li et

484   al., 2020), similar to our earlier observation in Yangzhou (0.75 $m^2\ g^{-1}$), but the $MAE_{365,}$

485    $_{MSOC}$ appears to be less than that in Yangzhou (1.12 $m^2\ g^{-1}$)(Chen et al., 2020). To further

486   explain the low MAE_{365} observed here, we investigated the air mass origins of our

487   samples collected in different periods via back trajectory analysis (at an altitude of 200

488   m and 24 hours backwards) using the MeteInfo (Version: 3.0.0) (Wang, 2019). As

489   shown in Fig. S6, only a limited fraction of air mass trajectories passed through sea and

490   coastal areas (clusters 4 and 5, 27.05 % during daytime and 29.54 % during nighttime)

491   during SS, while during CS, proportions of trajectories that intercepted sea/costal air

492   increased to 79.80 % (clusters 1, 2 and 3 during daytime) and 69.44% (clusters 2, 3 and

493   4 during nighttime), respectively. Note the air masses during CS are somewhat unusual

494   as typically they mainly originate from inland regions (Wu et al., 2019b), which might

495   cause the low MAE_{365} observed in this work as particles affected by marine air can be

496   less light-absorptive than those influenced by inland air (Li et al., 2022a).

497   Saleh (2020) proposes a method that uses the MAE_{405} (MAE at 405 nm) – AAE

498   two-dimension space to assess the light-absorbing ability of BrC, as shown in Fig. 4b.

499   The majority of samples in this study fall into the regime of W-BrC (weakly light-

500   absorptive BrC) with a few MSOC samples locating in the VW-BrC (very weak BrC)

501   regime, which are similar to a few other observations (Zhou et al., 2021; Xu et al., 2022).

502   The BrC in MSOC seemed to cover a broader region than it in WSOC, indicating that

503   the MSOC BrC might contain a wider array of species and/or originate from more

504   diverse sources/processes. Daytime/nighttime difference of MSOC BrC was also more

505   obvious than that of WSOC BrC.

506   At last, we estimated the SFE values of WSOC and MSOC in the range of 300–

507   700 nm, considering the actual visible light wavelength as well as the negligible light

508   absorption above 700 nm of BrC. As summarized in Table 1, the mean SFE_{MSOC} (2.43

509   W g^{-1}) during SS was higher than that of WSOC (2.20 W g^{-1}), but it became smaller

510   during CS (2.23 W g^{-1}) and was much lower than that of WSOC (3.24 W g^{-1}). The

511   SFE_{WSOC} values in both SS and CS were lower than that in Beijing (4.6 ± 1.7 W g^{-1} in

512   summer and 6.2 ± 2.0 W g^{-1} in winter), especially in CS (Deng et al., 2022). For both

513   WSOC and MSOC, SFE values during nighttime were slightly larger.

3.2.2 Source apportionment of light absorption of WSOC

515   In Sect. 3.1.2, sources of WSOA were identified and quantified, herein we applied

516   a multiple linear regression (MLR) algorithm to apportion the light absorption of

517   WSOC to these sources. The scatter plot of reconstructed $Abs_{365, WSOC}$ versus measured

518   values are shown in Fig. S7. The fitted slope is 1.06 with a Pearson's r of 0.90, verifying

519   the robustness of this method on our dataset. The calculated regression coefficients,

520   representing the factors' MAE_{365} values ($m^2\ g^{-1}$) are listed in Table 2. Compared to our

521   earlier results (Chen et al., 2020b), the HOA MAE_{365} (0.71 $m^2\ g^{-1}$), was much less than

522   that in Yangzhou (1.46 $m^2\ g^{-1}$), while the BBOA MAE_{365} values were similar (0.71 vs.

523   0.77); MAE_{365} values of OOA1 (0.12 $m^2\ g^{-1}$) and OOA2 (0.83 $m^2\ g^{-1}$) were very close

524   to the two SOA factors in Yangzhou (0.11 and 0.85 $m^2\ g^{-1}$). However, here the less

525   oxygented OOA1 has the small MAE_{365} while in Yangzhou, the more oxygenated SOA

526   has the similar MAE_{365} as OOA1, and *vice versa* for the other pair. This work finds that

527   the more oxidized SOA has a stronger light absorption ability, opposite to that reported

528   in Yangzhou. Nevertheless, the two findings are not contradictory with each other, as

529   atmospheric ageing can lead to either photo-enhancement or photo-bleachment,

530   dependent upon the precursors. For instances, aqueous oxidation of BBOA can increase

531   (Gilardoni et al., 2016) yet conversely aqueous processing of fossil fuel combustion OA

532   can decrease the light absorptivity of OA (Wang et al., 2021). As discussed in Sect.

533   3.2.1, the unusual air masses during CS in this work clearly indicate different precursors

534   from those in Yangzhou.

535   The average contributions of HOA, BBOA, OOA1 and OOA2 to $Abs_{365, WSOC}$

536   across the whole campaign were 33.05 %, 15.49 %, 6.00 % and 45.46 %, respectively

537   (Table 2). Figure 5 further presents contributions of the factors under different scenarios.

538   Compared with their mass contributions shown in Fig. 3a, during SS, the dominant

539   contributor of light absorption became HOA (daytime 63.7 %, nighttime 55.6 %), and

540   contributions of BBOA and OOA2 both increased relative to their mass fractions; while

541   OOA1's contribution was largely reduced to 15.0 ~ 16.2 % due to its small MAE_{365}.

542   Previous studies have consistently identified coal combustion (Fan et al., 2016; Li et al.,

543   2019; Song et al., 2019) and traffic emissions (Hecobian et al., 2010) as significant

544   contributors to BrC, together with our results here, highlighting the substantial impact

545   of anthropogenic fossil fuel combustion on atmospheric visibility. During CS, OOA2

546   dominated the light absorption (daytime 50.7 %, nighttme 63.0 %) owing to its large

547   mass contribution as well as large MAE_{365}; OOA1 became a very minor contributor

548   (2.1 ~ 2.8 %), HOA contribution decreased while BBOA contribution increased relative

549   to their mass fractions. Overall, we find that primary fossil fuel combustion emissions

550   govern water-soluble BrC light absorption during SS especailly during daytime, while

551   during CS, secondary highly aged species (likely from aqueous/heterogenous reactions)

552   dominates, especially during nighttime.

553   To further explore the impact of atmospheric ageing on BrC, we plotted MAE_{365}

554   as a function of O/C in Fig. 6. Interestingly, during SS, MAE_{365} generally decreased

555   with the increase of O/C, especially in daytime as its fitted slope of -1.56 was over 2

556   times that of nighttime (-0.76). On the other hand, MAE_{365} showed an increasing trend

557   against O/C during CS, particularly in nighttime as the fitted slope was 1.43, larger than

558   that of daytime (1.12). These results further supports our earlier findings and underscore

559   that during summer photochemical reactions can lead to photo-bleachment of aerosols

560   while during cold seasons aqueous/heterogenous reactions might dominate the

561   secondary formation and lead to photo-enhancement; clearly, photochemical oxidation

562   and aqueous/heterogenous reactions are more active during daytime and nighttime,

563 respectively, consistent with the slopes in Fig. 6. Also, photochemcially produced SOA

564 was often less or moderately oxygenated and that from aqueous/heteregenous oxidation

565 was more oxidized, and there is a turning point at O/C of 0.45 ~ 0.5 in the MAE_{365}-O/C

566 plot. Many studies have shown that aqueous reactions are a source of BrC (e.g., Li et

567 al. (2022c), Laskin et al. (2015) and Ye et al. (2019)), but evidence also shows that

568 further aqueous ageing of BrC can lead to photo-bleaching (e.g., Zhao et al. (2015) and

569 Lei et al. (2025)), therefore a certain O/C turning point can exist if the OA evolution

570 was governed by a certain process. The real atmospheric processes are however

571 complicated, such O/C points might be less clear. Nevertheless, similar points were

572 indeed observed previously (Zhong et al., 2023; Jiang et al., 2022).

3.2.3 Fluorescent properties of WSOC and MSOC

574 The fluorescence indices like HIX, BIX and FI, can infer the types and sources of

575 dissolved organic matter (DOM) in aquatic systems and soils (Lee et al., 2013; Huguet

576 et al., 2009). Recently, these indices have been employed to investigate sources and

577 aging processes of atmospheric OA (Fu et al., 2015; Qin et al., 2018; Deng et al., 2022;

578 Murphy et al., 2013). Here, we calculated these indices for both WSOC and MSOC.

579 HIX represents the degree of humification, and a high HIX means high

580 aggregation, C/H ratio and aromaticity of the organics (Zsolnay et al., 1999; Mcknight

581 et al., 2001; Birdwell and Engel, 2010), thus it normally increases upon ageing (Fan et

582 al., 2019; Murphy et al., 2013). In this study, HIX of WSOC during SS and CS were on

583 average 3.34 and 4.68, respectively (Table 3), much less than the HIX levels in aquatic

584 or soil DOM (Dong et al., 2017), suggesting an overall low aromaticity of atmospheric

585 OA in Nanjing. As a comparison, the WSOC HIX are higher than those in Colorado,

586 USA (2.42) (Xie et al., 2016) and Tianjin, China (2.73 and 2.22) (Deng et al., 2022),

587 but significantly lower than that in Nanjing during 2017-2018 (7.07) (Xie et al., 2020).

588 An earlier study proposes the HIX ranges of 1.4-5 for fresh SOA and 4.2-6.1 for aged

589 SOA (Lee et al., 2013). Despite influences of other primary sources, the average HIX

590 during SS did fall in the fresh SOA range and the value during CS entered the edge of

591 aged SOA, in line with the oxidation degrees of OA (Fig. 2a) and mass proportions of

592   fresh/aged SOA factors (namely, OOA1/OOA2) (Fig. 3a) during different seasons. The

593   average HIX of MSOC (2.72 and 3.48) were lower than those of WSOC in both seasons,

594   indicating that HULIS with high aromaticity are preferentially soluble in water.

595   FI is indicative of the relative contributions of terrestrial and biogenic sources

596   while BIX, in contrast to HIX, can be treated as a freshness index. A fluorophore is

597   often associated with high aromaticity if FI is low (Fu et al., 2015), and a high BIX

598   indicates a high content of freshly released organics (such as biological or microbial

599   derived species) (Wen et al., 2021; Huguet et al., 2009; Murphy et al., 2013). The

600   average WSOC BIX values during SS and CS were determined to be 0.84 and 0.88,

601   respectively, with corresponding FI of 1.91 and 1.90 (Table 3), and the corresponding

602   MSOC BIX were 0.90 and 0.96, and MSOC FI were 2.27 and 2.11, respectively.

603   Compared with results during 2017-2018 in Nanjing, BIX and FI values of WSOC were

604   similar, yet those of MSOC here were larger (Xie et al., 2020). Figure 7 shows the

605   measured data in the HIX-FI and HIX-BIX diagrams along with results from a few

606   other studies. It can be seen that, almost all BIX values distributed in the range of 0.6 ~

607   1 (Huguet et al., 2009) and FI values distributed within 1.6 ~ 1.9 (Mcknight et al., 2001),

608   suggesting that OA in both seasons was influenced by a mix of terrestrial and

609   microbial/biogenic sources. For both WSOC and MSOC, BIX was slightly higher

610   during CS than during SS, attributing to the fact that OA during CS contained more

611   aged SOA species. Nearly no difference for WSOC FI during different seasons were

612   observed, but the MSOC FI during CS was slightly lower than that during SS, meaning

613   that MSOC during CS had a high aromaticity as expected. In addition, BIX and FI

614   values during nighttime were marginally higher than those during daytime in all cases.

615   **3.2.4 Identification of key fluorophores of WSOC and MSOC**

616   The 3D EEM-PARAFAC analysis was adopted to identify the key fluorophores of

617   BrC, with results in Fig. 8 and Fig. S8. Four components were resolved for both WSOC

618   and MSOC. For WSOC, C1 exhibited a peak at Ex = 230 nm and Em = 374 nm,

619   identified as less oxidized HULIS typically associated with combustion sources. Its

620   contribution was only 4.9 % during SS but increased to 19.2 % during CS (Fig. S8a).

621 C2 had a prominent peak at Ex = 230 nm and Em = 396 nm and a second peak at Ex =

622 320 nm and Em = 396 nm, classified as a HULIS-related component too, as the dual-

623 peak distribution of fluorescence spectrum is often associated with HULIS (Coble,

624 1996; Murphy et al., 2011; Yu et al., 2015); its second peak indicates the abundance of

625 compounds with condensed aromatics, conjugated bonds, and non-linear rings (Matos

626 et al., 2015), likely a mix of primary and secondary sources. C2 contribution was thus

627 comparable during different seasons (37.5 % vs. 38.6 %), and it seemed to be more

628 important in nighttime than in daytime (44.0 % vs. 26.9 % during SS, and 41.4 % vs.

629 34.8 % during CS). C3 component, with a peak at Ex = 240 nm and Em = 446 nm, was

630 considered as a highly oxidized HULIS component, relevant with secondary processes

631 (Cheng et al., 2016; Cao et al., 2021). Hawkins et al. (2016) and Aiona et al. (2017)

632 reported fluorescent pattern of products from aqueous-phase reaction of aldehydes with

633 ammonium sulfate or amines (Ex < 250/300 nm and Em > 400 nm) well matching the

634 pattern identified here. As discussed earlier, aqueous/heterogenous reactions

635 contributed to WSOA, especaily during CS; correspondingly, C3 contribution was

636 indeed much higher during CS than during SS (24.1 % vs. 14.7 %). C4, with a

637 prominent peak at Ex = 230 nm and Em = 308 nm and a second peak at Ex = 275 nm

638 and Em = 305 nm, was characterized as a protein-like component (Yan and Kim, 2017;

639 Wu et al., 2019a; Chen et al., 2020b). C4 was the single largest contributor (42.9 %)

640 during SS particuly during daytime (55.0 %), but became the least during CS (18.0 %).

641 Similarly for MSOC, three HULIS-related fluorophores (C1 ~ C3) and one

642 proteinaceous fluorophore (C4) were separated (Fig. 8b). The spectral signatures

643 between the two series of fluorophores were slightly different, with the MSOC peak

644 excitation and emission wavelengths being a bit larger than those of WSOC, especially

645 for C2 and C3. Figure S8b shows contributions of the different components to MSOC

646 fluorescene. C1 was much more important in MSOC (26.6 % in SS and 39.2 % in CS)

647 than in WSOC, and became the largest contributor of MSOC during CS; summed C2

648 and C3 contributions (30.7 % in SS and 37.0 % in CS) were on the other hand much

649 less than in WSOC; C4 remained to be the largest (42.6 %) similar to that in WSOC

650 during SS. The increased contributions of the protein-like fluorophore (C4) during SS

651 in both WSOC and MSOC were likely due to its major origin of biological activities,

652 which can be enhanced by the relatively high temperatures during SS (Fan et al., 2020);

653 this is likely the reason that C4 contributions during daytime were higher than those

654 during nighttime in both SS and CS. Furthermore, some studies (Barsotti et al., 2016;

655 Chen et al., 2021; Chen et al., 2020b; Cao et al., 2021; Deng et al., 2022) also point out

656 that C4 not only contains proteinaceous species from biological activities but also

657 certain PAHs or phenolic substances from fossil fuel and/or biomass burning, especially

658 in urban aerosols. Probably, the proteinaceous species dominated the fluorescence

659 during SS for both WSOC and MSOC, while during CS PAHs and phenolic compounds

660 became more important and they might prefer to dissolve in methanol therefore lead to

661 its higher contribution in MSOC than in WSOC (23.8 % vs. 18.0 %). Different

662 solubilities of HULIS components in water and methanol may partially lead to their

663 different contributions in WSOC and MSOC.

664

665 **3.3 Molecular composition of organics**

666 **3.3.1 Overview of identified molecules**

667   We classified the identified molecular formulas of organics (here MSOA) via

668 UPLC-QTOF-MS analysis into 8 categories, namely CH, CHO, CHN, CHS, CHON,

669 CHOS, CHNS, and CHONS. Overall, the negative (ESI$^-$) and positive (ESI$^+$) ion modes

670 identified 466 ~ 865 and 644 ~ 1065 formulas, respectively (details in Table S1).

671 Figures S9 and S10 shows the number and signal fractions (relative abundances of

672 signal intensities) of different classes of compounds, respectively.

673   Under ESI$^+$ mode, CHON compounds were the most abundant species in term of

674 the number fraction – nearly half during SS (daytime 50.5 % and nighttime 46.9 %),

675 and over half during CS (daytime 54.1 % and nighttime 55.1 %), and the abundance of

676 its signal was even more prevailing – over half in all cases and up to 67.7 % during SS

677 daytime; the second abundant species were CHO compounds, occupying 23.0 ~ 30.6 %

678 of the total number of molecules and 15.4 ~ 21.9 % of the total signal intensity; CHONS

679 and CHN species were the other two relatively abundant classes – together occupying
680 ~ 20 % (number fraction) and ~ 10 ~ 24 % (signal fraction) of total identified
681 compounds; contributions of other four classes of compounds were very minor, in terms
682 of both number and signal intensity. Relatively, under ESI$^-$ mode, CHO compounds
683 marginally prevailed over CHON compounds in number (36.2 ~ 44.4 % vs. 32.6 ~
684 38.0 %), but during CS their signal fractions were still lower (33.3 ~ 35.1 % vs. 39.3 ~
685 46.5 %). More enrichment of CHO compounds in ESI$^-$ than in ESI$^+$ is consistent with
686 a previous work (Lin et al., 2012) as these compounds most likely contain carboxyl
687 groups and are easily deprotonated in ESI$^-$ mode. Number fractions of CHONS
688 compounds in ESI$^-$ mode were ~5 ~ 10% more than those in ESI$^+$ mode, while the most
689 contrasting difference was that CHN compounds were rarely detected in ESI$^+$ mode,
690 and instead CHOS compounds that were negligible in ESI$^-$ mode could be effectively
691 detected in ESI$^+$ mode (3.9 ~ 4.8 % in number) and their signal fractions were more
692 significant (6.4 ~ 17.4 %).

693 **3.3.2 CHO compounds**

694   For the detected CHO compounds, we plotted them in the van Krevelen (VK)
695 diagrams according to their H/C and O/C ratios in Fig. 9. Most molecules had the O/C
696 ratios < 0.5, but a broad distribution of H/C ratios (0.5 ~ 2.0). Molecules with high H/C
697 ratios ($\geq$ 1.5) and low O/C ratios ($\leq$ 0.5) (Region A) were typically associated with
698 aliphatic compounds, while those with low H/C ratios ($\leq$ 1.0) and low O/C ratios ($\leq$ 0.5)
699 (Region B) are usually assigned to oxygenated aromatics (Kourtchev et al., 2014). We
700 further calculated the Xc values of all CHO compounds to investigate their molecular
701 structures in Fig. 9. Clearly, saturated aliphatic CHO compounds (Xc < 2.5) were most
702 abundant (323 out of 418 in ESI$^+$ mode, and 315 out of 481 in ESI$^-$ mode) and mainly
703 distributed in Region A. Appreciate number of unsaturated compounds particularly
704 those with benzene ring or naphthalene ring structures (2.5 < Xc < 2.8), distributed
705 across from H/C of 0.5 to 1.75 but with O/C < 0.5 in ESI$^-$ mode and from H/C of 0.1 to
706 1.75 but with a few in the side of O/C > 0.5.

707   The oxygenation state (OS$_c$) (Kroll et al., 2011) (defined as 2*O/C - H/C), is

708 another metric to assess the ageing/oxidation degree of a compound. Figure 10

709 illustrates the dependence of OS_c on carbon number for all CHO compounds. The

710 molecules had a broad coverage of OS_c (-2 to +2) and carbon number (up to 50). Kroll

711 et al. (2011) grouped the compounds into different origins according to their OS_c and C

712 numbers, including fossil fuel combustion HOA, BBOA, semi-volatile oxygenated OA

713 (SV-OOA, typically less-oxidized) and low-volatility oxygenated OA (LV-OOA,

714 typically more-oxidized), as marked in Fig. 10. Obviously, for both ESI[-] and ESI[+]

715 modes, a large portion of compounds belonged to HOA and BBOA. In ESI[+] mode, a

716 significant portion of molecules located in the BBOA region, while in ESI[-] mode, more

717 molecules tended to be found in the HOA region, and even more molecules located

718 within HOA regime during CS than during SS (Figs. S11 and S12), indicating large

719 influences from anthropogenic emissions. Besides, the number of nighttime LV-OOA

720 molecules was more than that of daytime particular during CS, acting as a supporting

721 evidence of aqueous/heterogeneous reactions.

722 **3.3.3 CHON and CHN compounds**

723   We mapped the detected CHON compounds colored by Xc in the VK diagrams

724 shown in Fig. 11. The compounds were sorted into different series according to the

725 functional groups as well. For ESI[+] mode (Fig. 11a), the compounds containing a -NO

726 moiety were dominant and a majority of CHON compounds were saturated with Xc <

727 2.5. Among them, $C_6H_{15}NO(CH_2)_n$ might be N,N-diethylethanolamine homologous

728 compounds, and $C_6H_{15}NO_2(CH_2)_n$ might be diisopropanolamine homologous

729 compounds, as both compounds possess lone pair electrons, prone to positive charge

730 (Ge et al., 2011). Unsaturated CHON compounds with $X_C \geq 2.5$ located in the bottom-

731 left corner, such as $C_5H_5NO(CH_2)_n$, $C_7H_7NO(CH_2)_n$, $C_8H_7NO(CH_2)_n$, and

732 $C_9H_7NO(CH_2)_n$, likely homologous compounds of hydroxypyridine, benzamide,

733 4hydroxy-benzene acetonitrile, and hydroxyquinoline, respectively (Ma and Hays,

734 2008; Wang et al., 2020). In ESI[-] mode, the compounds scattered wider than those in

735 ESI[+] mode in the VK plot (Fig. 11b), and the majority of them contained one or two

736 nitrogen atoms. Over 25 % of the CHON formulas can be classified as monocyclic or

737 polycyclic compounds with Xc ≥ 2.5 (even up to 68 % during SS daytime; inferred

738 from Figs. S13 and S14). The identified series of homologous compounds mostly

739 situated in the bottom-left corner and also with Xc ≥ 2.5, such as $C_6H_5NO_3(CH_2)_n$,

740 $C_6H_5NO_4(CH_2)_n$, $C_8H_7NO_3(CH_2)_n$, $C_8H_7NO_4(CH_2)_n$, and $C_{10}H_7NO_3(CH_2)_n$, likely

741 nitrophenol, nitrocatechol, nitroacetophenone, nitrophenylacetic acid, and

742 nitronaphthol homologues, respectively (Wang et al., 2018b; Song et al., 2019; Lin et

743 al., 2017; Lin et al., 2015).

744 As stated in Sect. 3.3.1, CHN compounds were only enriched in ESI$^+$ mode. The

745 scatter plot of H/C versus N/C of these compounds is depicted in Fig. 12 (results of

746 different periods are shown in Fig. S15). Similarly, they are colored by Xc and sorted

747 into a number of different series. Most of these compounds were amines with one or

748 two N atoms. The series of aliphatic amines and other monocyclic species with $X_C <$

749 2.71 mostly located in upper part of the plot, including $C_6H_{15}N(CH_2)_n$, $C_5H_{11}N(CH_2)_n$

750 and $C_6H_{12}N(CH_2)_n$, $C_4H_6N_2(CH_2)_n$, $C_5H_6N_2(CH_2)_n$, $C_7H_6N_2(CH_2)_n$, and $C_{11}H_{17}N(CH_2)_n$.

751 Note the presence of 2 N-heterocyclic species was a sign of presence of BBOA (Wang

752 et al., 2017). The series of $C_{10}H_9N(CH_2)_n$ (1N-PAHs) with $X_C ≥ 2.71$ may represent the

753 aminonaphthalene homologues (Ge et al., 2011), likely from initial burning of

754 carbonaceous materials (Mao et al., 2022).

3.3.4 CHOS and CHONS compounds

756 Among the CHOS formulas (only significant in ESI$^-$ mode), ones with O/S ratios

757 ≥ 4 were classified as organosulfates (OSs), which were the most abundant type (Table

758 4). Its number fractions were particularly high during CS (daytime 54.3 %, nighttime

759 68.6 %), reiterating the importance of aqueous SOA formation during CS. For the

760 CHONS compounds, in ESI$^-$ mode, 5.3 ~ 12.5 % of the formulas had O/(4S+3N) ratios

761 ≥ 1, allowing them to be assigned to $-OSO_3H$ and $-ONO_2$ groups, namely nitrooxy-

762 organosulfates (nitrooxy-OSs) (Wang et al., 2018a); while in ESI$^+$ mode, 9.8 ~ 11.8%

763 of total CHONS formulas were apportioned as nitrooxy-OSs (Table 4).

764

3.4 Machine learning assisted identification of key BrC molecules

To enhance the robustness of ML analysis, we first incorporated all detected compounds without assigned molecular formulas of both positive and negative modes (4953 formulas, ESI⁺: 2863, ESI⁻: 2090) into the ML model. After ML analysis, a total of 1477 molecules (ESI⁺: 795; ESI⁻: 682) were found to have positive values for both IncNPu_val and IncMSE_val. Among them, 1051 molecules (ESI⁺: 420; ESI⁻: 450) were assigned corresponding molecular formulas; and furthermore, a total of 149 compounds with 0.5<DBE/C<0.9 (ESI⁺: 52; ESI⁻: 97) were chosen. By comparing with the database, we finally proposed 31 compounds (ESI⁺: 18, ESI⁻: 13) as the key BrC species; details regarding their molecular formulas and proposed structures, etc., are summarized in Table S2. These species are relevant with 4 out of 8 identified types of compounds (CH, CHO, CHN and CHON) (Fig. 13). To the best of our knowledge, 6 out of the 31 species (4-methylcoumarin, urocanate, 3-hydroxybenzoic acid, chrysin, 2-hydroxypyridine and 4-hydroxyacetophenone) have not been reported before as important BrC species.

Two PAHs (acenapthylene and fluoranthene, belonging to CH category) in ESI⁺ mode were identified, consistent with that PAHs are known important BrC (Aurell et al., 2015; Kuang et al., 2021).

Twelve CHO compounds (5 in ESI⁺ mode and 7 in ESI⁻ mode) were identified. In ESI⁺ mode, 9-fluorenone and benzanthrone belonging to oxyheterocyclic PAHs (O-PAHs), are known as important BrC chromophores (Kuang et al., 2023); scopoletin is also known as a light-absorbing compound (Zhang, 2018); phthalic anhydride is an oxygen-containing heterocyclic compound. A previous study reports that methanol (the solvent used here) might react with conjugated carbonyl species (such as phthalic anhydride, maleic anhydride, and maleimide) (Chen et al., 2022), thereby affecting the light absorption of relevant BrC species, further studies are needed to verify phthalic anhydride as a key chromophore. In ESI⁻ mode, a pair of quinone isomers (1-hydroxyanthraquinone and 2-hydroxyanthraquinone) were resolved, in agreement with Kuang et al. (2023), which identified 1-hydroxyanthraquinone as a BrC chromophore

794   in Beijing; 1-hydroxypyrene is a hydroxylated PAHs , also proven as a BrC before
795   (Huang et al., 2022).

796   The identified seven CHN compounds (exclusively in ESI$^+$ mode) included 4 N-
797   heterocyclics, 2 nitro-PAHs, and 1 quinoline compound. It is well known that biomass
798   burning (BB) release a lot of BrC species. As mentioned earlier, CHN compounds are
799   abundant in BB emissions (such as agricultural waste burning and forest fires (Laskin
800   et al., 2009)); small N-containing heterocyclic compounds with one or two aromatic
801   rings, can be effectively produced from thermal decomposition of plants (Ma and Hays,
802   2008), and high temperature pyrolysis of CHN compounds and N-containing plant
803   materials, can result in N-PAHs (Lin et al., 2016). Therefore, identification of the CHN
804   species here as key BrC chromophores are well justified.

805   The remaining confirmed BrC molecules included 10 CHON compounds (4 in
806   ESI$^+$ mode and 6 in ESI$^-$ mode). For ESI$^-$ mode, 3-hydroxyanthranilic acid is an amino
807   phenolic compound $^-$, and the rest five compounds are all nitrophenols, well known as
808   BrC (Li et al., 2020). Another amino phenolic compound, 2-aminophenol was identified
809   in ESI$^+$ mode. Previously, efficient light absorption at 275 nm of 2-aminophenol has
810   been reported, which can be further enhanced in the presence of Fe^{3+} due to formation
811   of oligomers (Al-Abadleh et al., 2022). For acridone in ESI$^+$ mode, earlier studies have
812   shown that acridine exhibits increased light absorbance in the wavelength range of 260
813    $\sim$ 320 nm under irradiation in N$_2$, air, or O$_2$; additionally, a deep yellow layer forms on
814   the surface, indicating the production of light-absorbing products, which was identified
815   as acridone (Negron-Encarnacion and Arce, 2007).

816   For the BrC species identified here, most species contain at least one benzene ring
817   (such as PAHs and NACs) except two compounds (2-hydroxypyridine and urocanate)
818   with other aromatic ring structures. This is reasonable as organic compounds with
819   benzene or other aromatic rings (with conjugated double bonds) are known to be strong
820   light-absorbing. The -OH and -COOH groups on the benzene ring can enhance
821   ultraviolet light absorption at near-UV wavelengths (Jacobson, 1999); The -NO$_2$ group
822   can further increase light absorbance at longer wavelengths (Jacobson, 1999). Our

823   identified BrC list does include compounds with such functional groups. Note some

824   nitrogen-containing heterocyclic compounds, are usually secondary products of

825   aqueous reactions between carbonyl compounds (such as glyoxal and methylglyoxal)

826   and amines or ammonium (Powelson et al., 2014); thus identification of them here as

827   key BrC species is also a supporting evidence of the occurrence of aqueous reactions.

828

829   **4 Conclusions**

830   This work performed a comprehensive investigation on the chemical and optical

831   properties of BrC in ambient $PM_{2.5}$ samples. Regarding the chemical properties, it was

832   found that methanol was able to extract more OC than water (~82.0% vs. 49.5 ~ 61.3%

833   of total OC). The WSOA was composed of two primary factors relevant with fossil fuel

834   combustion (HOA) and biomass burning (BBOA), and two SOA factors (a less oxidized

835   OOA1 and a highly oxygenated OOA2). During CS, OOA2 was abundant (38.6 ~

836   43.5 %) while during SS OOA1 was abundant (47.5 ~ 49.8 %); HOA was also an

837   important contributor in both seasons (29.9 ~ 41.7%) but BBOA contribution was

838   relatively minor (7.2 ~ 13.0 %). Further analyses reveal that OOA1 was mainly

839   associated with photochemical reactions while OOA2 was strongly linked with

840   aqueous/heterogeneous reactions.

841   Regarding the optical properties, our observation shows that $Abs_{365,\ MSOC}$ was

842   typically larger than $Abs_{365,\ WSOC}$, but though $MAE_{365,\ MSOC}$ was still larger than $MAE_{365,}$

843     $_{WSOC}$ during SS, it became smaller than the $MAE_{365,\ WSOC}$ during CS, likely owing to

844   that the air mass trajectories during CS significantly intercepted sea/coastal air. The

845   light absorbing abilities of both WSOC and MSOC were weak, but our observations

846   suggest that aqueous oxidation can lead to significant photo-enhancement, therefore the

847   light absorption of WSOA was dominated by OOA2 (50.7 ~ 63.0 %) during CS; while

848   photochemical oxidation could cause a photo-bleaching effect and therefore the

849   contribution of OOA1 to WSOA absorbance was small (15.0 ~ 16.2 %), and HOA

850   contribution was prevailing during SS (55.6 ~ 63.7 %). PARAFAC analysis on the

851   fluorescent spectra of WSOC and MSOC both resolved four key components, including

852 three HULIS component and one protein-like component. HIX, BIX and FI indices also
853 suggest that both WSOC and MSOC originated from a mix of terrestrial and
854 microbial/biogenic sources.

855 The molecular analysis determined 644 ~ 1065 molecules in ESI^+ mode and 466 ~
856 865 molecules in ESI^- mode. Overall, CHON compounds were the most abundant type
857 especially in ESI^+ mode, while CHO compounds slightly exceeded CHON compounds
858 in number but were still lower in signal intensity. CHN compounds was the third
859 important class and only detectable in ESI^+ mode. The VK diagrams further
860 demonstrate the different aromaticity equivalent (Xc) values and evolution pathways of
861 the different classes of compounds. In addition, significant presence of organosulfates
862 and nitroxy-organosulfates in CS samples especially during nighttime re-affirm the
863 importance of aqueous-phase oxidation during CS. Finally, based on the molecular
864 characterization and light absorption measurement results, we applied the ML RF
865 algorithm to identify the key BrC molecules, and we successfully identified 31 key
866 species, including mainly the PAHs, oxyheterocyclic PAHs (O-PAHs), quinones and N-
867 containing compounds; some of them are newly identified.

868 Of course, our study has some limitations. One limitation is that no source
869 apportionment was conducted on MSOA due to technical difficulties, therefore a full
870 closure between emission sources and optical properties of total OA is incomplete;
871 development of proper method should be the subject of our future work.
872 ~~Moreover~~Besides, our findings here expand the understanding on chemical (both bulk
873 and molecular level) and optical properties (both light absorption and fluorescence) of
874 BrC, and are valuable to evaluate its impact on air quality and radiation balance; ~~the~~
875 ~~identified list of key BrC molecules can be a useful reference for future studies.~~
876 ~~However,~~yet our practice with ML ~~approach~~analysis here serves ~~as~~ only ~~a case study~~
877 ~~and~~as a valuable attempt, more studies ~~likely with more advanced ML algorithms~~ are
878 clearly needed ~~to identify more BrC species, and to achieve a quantitative closure~~
879 ~~between the BrC molecules and its total light absorption.~~.

880

881   Nevertheless, the ML approach has demonstrated its great potential in identifying
882 new key BrC species (such as 4-methylcoumarin, urocanate, etc here) as well as
883 reaffirming the importance of known key BrC molecules (such as the nitrogen-
884 containing aromatic molecules); such ML-identified list can be a useful reference for
885 future studies. Of course, since there are multiple types of ML algorithms (such as
886 supervised, unsupervised, semisupervised and reinforcement learning) with differing
887 key parameters, performances as well as advantages/pitfalls in environmental research
888 (Zhu et al., 2023), the rigorous, accurate, robust and also practicable ML analysis
889 requires more research efforts and will be an active and important topic in the future.
890 The ML approach can be a powerful and promising tool to achieve a quantitative closure
891 between the BrC molecules and its total light absorption.

892 **Code availability.** The software code to analyze the SP-AMS data is publicly available
893 at: https://cires1.colorado.edu/jimenez-
894 group/ToFAMSResources/ToFSoftware/index.html. The software code to analyze the
895 UPLC-QTOF-MS data is publicly available at:
896 https://systemsomicslab.github.io/compms/msdial/main.html. The software code using
897 SERRF to normalize UPLC-QTOF-MS data is available at:
898 https://slfan.shinyapps.io/ShinySERRF/

899

900 **Data availability.** The data in this study are available from the authors upon request
901 (caxinra@163.com).

902

903 **Supplement.** The supplement related to this article is available online at: XXX

904

905 **Author contributions.** YH, XL and DDH conducted the experiments. YH, XL, RL,
906 BZ, YZ and XG performed the data analysis. YH and XG wrote the paper. All authors
907 reviewed the paper and provide useful suggestions.

908

909 **Competing interests.** The contact author has declared that neither they nor their co-

910 authors have any competing interests.

911

912 **Disclaimer.** Publisher's note: Copernicus Publications remains neutral with regard to

913 jurisdictional claims in published maps and institutional affiliations.

914

915 **Acknowledgements.** We sincerely thank the logistic help from the Center for

916 Experimental Atmospheric Science and Environmental Meteorology of Nanjing

917 University of Information Science and Technology (NUIST) during sampling.

918

919 **Financial support.** This work has been supported by the National Natural Science

920 Foundation of China (grant nos. 22361162668 and 42021004).

921

922 **Review statement.** This paper was edited by XXX, and XXX.

923

References

925 Aiken, A. C., DeCarlo, P. F., Kroll, J. H., Worsnop, D. R., Huffman, J. A., Docherty,

926 K. h. S., Ulbrich, I. M., Mohr, C., Kimmel, J. l. R., Sueper, D., Sun, Y. l., Zhang, Q.,

927 Trimborn, A., Northway, M., Ziemann, P. J., Canagaratna, M. a. R., Onasch, T. B.,

928 Alfarra, M. R., Prevot, A. S. H., Dommen, J., Duplissy, J., Metzger, A., Baltensperger,

929 U., and Jimenez, J. L.: O/C and OM/OC ratios of primary, secondary, and ambient

930 organic aerosols with high-resolution time-of-flight aerosol mass spectrometry, Environ.

931 Sci. Technol., 42, 4478-4485, https://doi.org/10.1021/es703009q, 2008.

932 Aiona, P. K., Lee, H. J., Leslie, R., Lin, P., Laskin, A., Laskin, J., and Nizkorodov,

933 S. A.: Photochemistry of products of the aqueous reaction of methylglyoxal with

934 ammonium sulfate, ACS Earth Space Chem., 1, 522-532,

935 https://doi.org/10.1021/acsearthspacechem.7b00075, 2017.

936 Al-Abadleh, H. A., Motaghedi, F., Mohammed, W., Rana, M. S., Malek, K. A.,

937 Rastogi, D., Asa-Awuku, A. A., and Guzman, M. I.: Reactivity of aminophenols in

938 forming nitrogen-containing brown carbon from iron-catalyzed reactions, Commun.

Chem., 5, 112, https://doi.org/10.1038/s42004-022-00732-1, 2022.

Andreae, M. O. and Gelencsér, A.: Black carbon or brown carbon? The nature of light-absorbing carbonaceous aerosols, Atmos. Chem. Phys., 6, 3131-3148, https://doi.org/10.5194/acp-6-3131-2006, 2006.

Aurell, J., Gullett, B. K., and Tabor, D.: Emissions from southeastern U.S. Grasslands and pine savannas: Comparison of aerial and ground field measurements with laboratory burns, Atmos. Environ., 111, 170-178, https://doi.org/10.1016/j.atmosenv.2015.03.001, 2015.

Bae, E., Yeo, I. J., Jeong, B., Shin, Y., Shin, K. H., and Kim, S.: Study of double bond equivalents and the numbers of carbon and oxygen atom distribution of dissolved organic matter with negative-mode FT-ICR MS, Analytical Chemistry, 83, 4193-4199, https://doi.org/10.1021/ac200464q, 2011.

Bai, D. P., Wang, H. L., Tan, Y., Yin, Y., Wu, Z. J., Guo, S., Shen, L. J., Zhu, B., Wang, J. H., and Kong, X. C.: Optical properties of aerosols and chemical composition apportionment under different pollution levels in Wuhan during January 2018, https://doi.org/10.3390/atmos11010017, 2020.

Barsotti, F., Ghigo, G., and Vione, D.: Computational assessment of the fluorescence emission of phenol oligomers: A possible insight into the fluorescence properties of humic-like substances (HULIS), J. Photochem. Photobiol., A, 315, 87-93, https://doi.org/10.1016/j.jphotochem.2015.09.012, 2016.

Bhowmik, H. S., Tripathi, S. N., Shukla, A. K., Lalchandani, V., Murari, V., Devaprasad, M., Shivam, A., Bhushan, R., Prévôt, A. S. H., and Rastogi, N.: Contribution of fossil and biomass-derived secondary organic carbon to winter water-soluble organic aerosols in Delhi, India, Sci. Total Environ., 912, 168655, https://doi.org/10.1016/j.scitotenv.2023.168655, 2024.

Birdwell, J. E. and Engel, A. S.: Characterization of dissolved organic matter in cave and spring waters using UV–Vis absorbance and fluorescence spectroscopy, Org. Geochem., 41, 270-280, https://doi.org/10.1016/j.orggeochem.2009.11.002, 2010.

Bond, T. C. and Bergstrom, R. W.: Light absorption by carbonaceous particles: an investigative review, Aerosol Sci. Technol., 40, 27-67, https://doi.org/10.1080/02786820500421521, 2006.

Bones, D. L., Henricksen, D. K., Mang, S. A., Gonsior, M., Bateman, A. P., Nguyen, T. B., Cooper, W. J., and Nizkorodov, S. A.: Appearance of strong absorbers and fluorophores in limonene-O3 secondary organic aerosol due to NH4+-mediated chemical aging over long time scales, J. Geophys. Res.: Atmos., 115, https://doi.org/10.1029/2009JD012864, 2010.

Bozzetti, C., El Haddad, I., Salameh, D., Daellenbach, K. R., Fermo, P., Gonzalez, R., Minguillón, M. C., Iinuma, Y., Poulain, L., Elser, M., Müller, E., Slowik, J. G., Jaffrezo, J. L., Baltensperger, U., Marchand, N., and Prévôt, A. S. H.: Organic aerosol source apportionment by offline-AMS over a full year in Marseille, Atmos. Chem. Phys., 17, 8247-8268, https://doi.org/10.5194/acp-17-8247-2017, 2017.

Brown, H., Wang, H. L., Flanner, M., Liu, X. H., Singh, B., Zhang, R. D., Yang, Y., and Wu, M. X.: Brown Carbon Fuel and Emission Source Attributions to Global Snow Darkening Effect, J ADV MODEL EARTH SY, 14, https://doi.org/10.1029/2021ms002768, 2022.

Budisulistiorini, S. H., Riva, M., Williams, M., Chen, J., Itoh, M., Surratt, J. D., and Kuwata, M.: Light-absorbing brown carbon aerosol constituents from combustion of indonesian peat and biomass, Environ. Sci. Technol., 51, 4415-4423, https://doi.org/10.1021/acs.est.7b00397, 2017.

Cain, J., Laskin, A., Kholghy, M. R., Thomson, M. J., and Wang, H.: Molecular characterization of organic content of soot along the centerline of a coflow diffusion flame, Phys. Chem. Chem. Phys., 16, 25862-25875, https://doi.org/10.1039/C4CP03330B, 2014.

Canagaratna, M. R., Jayne, J. T., Ghertner, D. A., Herndon, S., Shi, Q., Jimenez, J. L., Silva, P. J., Williams, P., Lanni, T., Drewnick, F., Demerjian, K. L., Kolb, C. E., and Worsnop, D. R.: Chase studies of particulate emissions from in-use New York City vehicles, Aerosol Sci. Technol., 38, 555-573,

996 https://doi.org/10.1080/02786820490465504, 2004.

997 Canagaratna, M. R., Jimenez, J. L., Kroll, J. H., Chen, Q., Kessler, S. H., Massoli,

998 P., Hildebrandt Ruiz, L., Fortner, E., Williams, L. R., Wilson, K. R., Surratt, J. D.,

999 Donahue, N. M., Jayne, J. T., and Worsnop, D. R.: Elemental ratio measurements of

1000 organic compounds using aerosol mass spectrometry: characterization, improved

1001 calibration, and implications, Atmos. Chem. Phys., 15, 253-272,

1002 https://doi.org/10.5194/acp-15-253-2015, 2015.

1003 Cao, T., Li, M. J., Zou, C. L., Fan, X. J., Song, J. Z., Jia, W. L., Yu, C. L., Yu, Z.

1004 Q., and Peng, P. A.: Chemical composition, optical properties, and oxidative potential

1005 of water- and methanol-soluble organic compounds emitted from the combustion of

1006 biomass materials and coal, Atmos. Chem. Phys., 21, 13187-13205,

1007 https://doi.org/10.5194/acp-21-13187-2021, 2021.

1008 Cavalli, F., Facchini, M. C., Decesari, S., Mircea, M., Emblico, L., Fuzzi, S.,

1009 Ceburnis, D., Yoon, Y. J., O'Dowd, C. D., Putaud, J. P., and Dell'Acqua, A.: Advances

1010 in characterization of size-resolved organic matter in marine aerosol over the North

1011 Atlantic, J. Geophys. Res.: Atmos., 109, https://doi.org/10.1029/2004JD005137, 2004.

1012 Chakrabarty, R. K., Moosmüller, H., Chen, L. W. A., Lewis, K., Arnott, W. P.,

1013 Mazzoleni, C., Dubey, M. K., Wold, C. E., Hao, W. M., and Kreidenweis, S. M.: Brown

1014 carbon in tar balls from smoldering biomass combustion, Atmos. Chem. Phys., 10,

1015 6363-6370, https://doi.org/10.5194/acp-10-6363-2010, 2010.

1016 Chakrabarty, R. K., Shetty, N. J., Thind, A. S., Beeler, P., Sumlin, B. J., Zhang, C.,

1017 Liu, P., Idrobo, J. C., Adachi, K., Wagner, N. L., Schwarz, J. P., Ahern, A., Sedlacek, A.

1018 J., 3rd, Lambe, A., Daube, C., Lyu, M., Liu, C., Herndon, S., Onasch, T. B., and Mishra,

1019 R.: Shortwave absorption by wildfire smoke dominated by dark brown carbon, Nat

1020 Geosci, 16, 683-688, https://doi.org/10.1038/s41561-023-01237-9, 2023.

1021 Chen, K. P., Raeofy, N., Lum, M., Mayorga, R., Woods, M., Bahreini, R., Zhang,

1022 H. F., and Lin, Y. H.: Solvent effects on chemical composition and optical properties of

1023 extracted secondary brown carbon constituents, Aerosol Sci. Technol., 56, 917-930,

1024 https://doi.org/10.1080/02786826.2022.2100734, 2022.

Chen, Q. C., Hua, X. Y., Li, J. W., Chang, T., and Wang, Y. Q.: Diurnal evolutions and sources of water-soluble chromophoric aerosols over Xi'an during haze event, in Northwest China, Sci. Total Environ., 786, 147412, https://doi.org/10.1016/j.scitotenv.2021.147412, 2021.

Chen, Q. C., Li, J. W., Hua, X. Y., Jiang, X. T., Mu, Z., Wang, M. M., Wang, J., Shan, M., Yang, X. D., Fan, X. J., Song, J. Z., Wang, Y. Q., Guan, D. J., and Du, L.: Identification of species and sources of atmospheric chromophores by fluorescence excitation-emission matrix with parallel factor analysis, Sci. Total Environ., 718, 137322, https://doi.org/10.1016/j.scitotenv.2020.137322, 2020a.

Chen, Q. C., Miyazaki, Y., Kawamura, K., Matsumoto, K., Coburn, S., Volkamer, R., Iwamoto, Y., Kagami, S., Deng, Y. G., Ogawa, S. H., Ramasamy, S., Kato, S., Ida, A., Kajii, Y., and Mochida, M.: Characterization of chromophoric water-soluble organic matter in urban, forest, and marine aerosols by HR-ToF-AMS analysis and excitation–emission matrix spectroscopy, Environ. Sci. Technol., 50, 10351-10360, https://doi.org/10.1021/acs.est.6b01643, 2016.

Chen, Y. and Bond, T. C.: Light absorption by organic carbon from wood combustion, Atmos. Chem. Phys., 10, 1773-1787, https://doi.org/10.5194/acp-10-1773-2010, 2010.

Chen, Y. F., Ge, X. L., Chen, H., Xie, X. C., Chen, Y. T., Wang, J. F., Ye, Z. L., Bao, M. Y., Zhang, Y. L., and Chen, M. D.: Seasonal light absorption properties of water-soluble brown carbon in atmospheric fine particles in Nanjing, China, Atmos. Environ., 187, 230-240, https://doi.org/10.1016/j.atmosenv.2018.06.002, 2018.

Chen, Y. F., Xie, X. C., Shi, Z., Li, Y. L., Gai, X. Y., Wang, J. F., Li, H. W., Wu, Y., Zhao, X. Y., Chen, M. D., and Ge, X. L.: Brown carbon in atmospheric fine particles in Yangzhou, China: Light absorption properties and source apportionment, Atmos. Res., 244, 105028, https://doi.org/10.1016/j.atmosres.2020.105028, 2020b.

Cheng, Y., He, K. B., Du, Z. Y., Engling, G., Liu, J. M., Ma, Y. L., Zheng, M., and Weber, R. J.: The characteristics of brown carbon aerosol during winter in Beijing, Atmos. Environ., 127, 355-364, https://doi.org/10.1016/j.atmosenv.2015.12.035, 2016.

1054   Coble, P. G.: Characterization of marine and terrestrial DOM in seawater using

1055   excitation-emission matrix spectroscopy, Mar. Chem., 51, 325-346,

1056   https://doi.org/10.1016/0304-4203(95)00062-3, 1996.

1057   Daellenbach, K. R., Stefenelli, G., Bozzetti, C., Vlachou, A., Fermo, P., Gonzalez,

1058   R., Piazzalunga, A., Colombi, C., Canonaco, F., Hueglin, C., Kasper-Giebl, A., Jaffrezo,

1059   J. L., Bianchi, F., Slowik, J. G., Baltensperger, U., El-Haddad, I., and Prévôt, A. S. H.:

1060   Long-term chemical analysis and organic aerosol source apportionment at nine sites in

1061   central Europe: source identification and uncertainty assessment, Atmos. Chem. Phys.,

1062   17, 13265-13282, https://doi.org/10.5194/acp-17-13265-2017, 2017.

1063   DeLessio, M. A., Tsigaridis, K., Bauer, S. E., Chowdhary, J., and Schuster, G. L.:

1064   Modeling atmospheric brown carbon in the GISS ModelE Earth system model, Atmos.

1065   Chem. Phys., 24, 6275-6304, https://doi.org/10.5194/acp-24-6275-2024, 2024.

1066   Deng, J. J., Ma, H., Wang, X. F., Zhong, S. J., Zhang, Z. M., Zhu, J. L., Fan, Y. B.,

1067   Hu, W., Wu, L. B., Li, X. D., Ren, L. J., Pavuluri, C. M., Pan, X. L., Sun, Y. L., Wang,

1068   Z. F., Kawamura, K., and Fu, P. Q.: Measurement report: Optical properties and sources

1069   of water-soluble brown carbon in Tianjin, North China – insights from organic

1070   molecular compositions, Atmos. Chem. Phys., 22, 6449-6470,

1071   https://doi.org/10.5194/acp-22-6449-2022, 2022.

1072   Dey, S., Mukherjee, A., Polana, A. J., Rana, A., Mao, J. Y., Jia, S. G., Yadav, A. K.,

1073   Khillare, P. S., and Sarkar, S.: Brown carbon aerosols in the Indo-Gangetic Plain

1074   outflow: insights from excitation emission matrix (EEM) fluorescence spectroscopy,

1075   Environ. Sci.: Processes Impacts, 23, 745-755, https://doi.org/10.1039/D1EM00050K,

1076   2021.

1077   Dong, W. M., Wan, J. M., Tokunaga, T. K., Gilbert, B., and Williams, K. H.:

1078   Transport and humification of dissolved organic matter within a semi-arid floodplain,

1079   J. Environ. Sci, 57, 24-32, https://doi.org/10.1016/j.jes.2016.12.011, 2017.

1080   Dührkop, K., Fleischauer, M., Ludwig, M., Aksenov, A. r. A., Melnik, A. V.,

1081   Meusel, M., Dorrestein, P. r. C., Rousu, J., and Böcker, S.: SIRIUS 4: a rapid tool for

turning tandem mass spectra into metabolite structure information, Nat. Methods, 16, 299-302, https://doi.org/10.1038/s41592-019-0344-8, 2019.

Fan, X. J., Wei, S. Y., Zhu, M. B., Song, J. Z., and Peng, P. A.: Comprehensive characterization of humic-like substances in smoke PM2.5 emitted from the combustion of biomass materials and fossil fuels, Atmos. Chem. Phys., 16, 13321-13340, https://doi.org/10.5194/acp-16-13321-2016, 2016.

Fan, X. J., Yu, X. F., Wang, Y., Xiao, X., Li, F. Y., Xie, Y., Wei, S. Y., Song, J. Z., and Peng, P. A.: The aging behaviors of chromophoric biomass burning brown carbon during dark aqueous hydroxyl radical oxidation processes in laboratory studies, Atmos. Environ., 205, 9-18, https://doi.org/10.1016/j.atmosenv.2019.02.039, 2019.

Fan, Y., Liu, C. Q., Li, L., Ren, L., Ren, H., Zhang, Z., Li, Q., Wang, S., Hu, W., Deng, J., Wu, L., Zhong, S., Zhao, Y., Pavuluri, C. M., Li, X., Pan, X., Sun, Y., Wang, Z., Kawamura, K., Shi, Z., and Fu, P.: Large contributions of biogenic and anthropogenic sources to fine organic aerosols in Tianjin, North China, Atmos. Chem. Phys., 20, 117-137, https://doi.org/10.5194/acp-20-117-2020, 2020.

Fasola, S., Maio, S., Baldacci, S., La Grutta, S., Ferrante, G., Forastiere, F., Stafoggia, M., Gariazzo, C., and Viegi, G.: Effects of particulate matter on the incidence of respiratory diseases in the pisan longitudinal study, Int. J. Environ. Res. Public Health, 17, https://doi.org/10.3390/ijerph17072540, 2020.

Feng, Y., Ramanathan, V., and Kotamarthi, V. R.: Brown carbon: a significant atmospheric absorber of solar radiation?, Atmos. Chem. Phys., 13, 8607-8621, https://doi.org/10.5194/acp-13-8607-2013, 2013.

Fleming, L. T., Lin, P., Roberts, J. M., Selimovic, V., Yokelson, R., Laskin, J., Laskin, A., and Nizkorodov, S. A.: Molecular composition and photochemical lifetimes of brown carbon chromophores in biomass burning organic aerosol, Atmos. Chem. Phys., 20, 1105-1129, https://doi.org/10.5194/acp-20-1105-2020, 2020.

Fu, P. Q., Kawamura, K., Chen, J., Qin, M. Y., Ren, L. J., Sun, Y. L., Wang, Z. F., Barrie, L. A., Tachibana, E., Ding, A. J., and Yamashita, Y.: Fluorescent water-soluble organic aerosols in the High Arctic atmosphere, Sci. Rep., 5, 9845,

https://doi.org/10.1038/srep09845, 2015.

Ge, X. L., Wexler, A. S., and Clegg, S. L.: Atmospheric amines – part I. a review, Atmos. Environ., 45, 524-546, https://doi.org/10.1016/j.atmosenv.2010.10.012, 2011.

Ge, X. L., Sun, Y. L., Trousdell, J., Chen, M. D., and Zhang, Q.: Enhancing characterization of organic nitrogen components in aerosols and droplets using high-resolution aerosol mass spectrometry, Atmos. Meas. Tech., 17, 423-439, https://doi.org/10.5194/amt-17-423-2024, 2024.

Ge, X. L., Li, L., Chen, Y. F., Chen, H., Wu, D., Wang, J. F., Xie, X. C., Ge, S., Ye, Z. L., Xu, J. Z., and Chen, M. D.: Aerosol characteristics and sources in Yangzhou, China resolved by offline aerosol mass spectrometry and other techniques, Environ. Pollut., 225, 74-85, https://doi.org/10.1016/j.envpol.2017.03.044, 2017.

Gilardoni, S., Massoli, P., Paglione, M., Giulianelli, L., Carbone, C., Rinaldi, M., Decesari, S., Sandrini, S., Costabile, F., Gobbi, G. P., Pietrogrande, M. C., Visentin, M., Scotto, F., Fuzzi, S., and Facchini, M. C.: Direct observation of aqueous secondary organic aerosol from biomass-burning emissions, Proc. Natl. Acad. Sci. U. S. A., 113, 10013-10018, https://doi.org/10.1073/pnas.1602212113, 2016.

González, C., Mira-M., J., and Juárez, I.: Important variable assessment and electricity price forecasting based on regression tree models: classification and regression trees, Bagging and Random Forests, IET Gener. Transm. Dis., 9, 1120-1128, https://doi.org/10.1049/iet-gtd.2014.0655, 2015.

Gu, C. J., Cui, S. J., Ge, X. L., Wang, Z. Y., Chen, M. J., Qian, Z. H., Liu, Z. Y., Wang, X. F., and Zhang, Y. J.: Chemical composition, sources and optical properties of nitrated aromatic compounds in fine particulate matter during winter foggy days in Nanjing, China, Environ. Res., 212, 113255, https://doi.org/10.1016/j.envres.2022.113255, 2022.

Hawkins, L. N., Lemire, A. N., Galloway, M. M., Corrigan, A. L., Turley, J. J., Espelien, B. M., and De H., D. O.: Maillard chemistry in clouds and aqueous aerosol as a source of atmospheric humic-like substances, Environ. Sci. Technol., 50, 7443-7452, https://doi.org/10.1021/acs.est.6b00909, 2016.

1140   Hecobian, A., Zhang, X., Zheng, M., Frank, N., Edgerton, E. S., and Weber, R. J.:

1141   Water-soluble organic aerosol material and the light-absorption characteristics of

1142   aqueous extracts measured over the southeastern united states, Atmos. Chem. Phys., 10,

1143   5965-5977, https://doi.org/10.5194/acp-10-5965-2010, 2010.

1144   Hu, J. L., Wang, P., Ying, Q., Zhang, H. L., Chen, J. J., Ge, X. L., Li, X. H., Jiang,

1145   J. K., Wang, S. X., Zhang, J., Zhao, Y., and Zhang, Y. Y.: Modeling biogenic and

1146   anthropogenic secondary organic aerosol in China, Atmos. Chem. Phys., 17, 77-92,

1147   https://doi.org/10.5194/acp-17-77-2017, 2017.

1148   Hu, R. L., Xu, Q. C., Wang, S. X., Hua, Y., Bhattarai, N., Jiang, J K., Song, Y.,

1149   Daellenbach, K. R., Qi, L., Prevot, A. S. H., and Hao, J. M.: Chemical characteristics

1150   and sources of water-soluble organic aerosol in southwest suburb of Beijing, J. Environ.

1151   Sci., 95, 99-110, https://doi.org/10.1016/j.jes.2020.04.004, 2020.

1152   Huang, L. B., Liu, T. S., and Grassian, V. i. H.: Radical-Initiated formation of

1153   aromatic organosulfates and sulfonates in the aqueous phase, Environ. Sci. Technol.,

1154   54, 11857-11864, https://doi.org/10.1021/acs.est.0c05644, 2020.

1155   Huang, R. J., Yang, L., Shen, J. C., Yuan, W., Gong, Y. Q., Ni, H. Y., Duan, J., Yan,

1156   J., Huang, H. B., You, Q. H., and Li, Y., J.: Chromophoric fingerprinting of brown

1157   carbon from residential biomass burning, Environ. Sci. Technol. Lett., 9, 102-111,

1158   https://doi.org/10.1021/acs.estlett.1c00837, 2022.

1159   Huang, R. J., Yang, L., Cao, J. J., Chen, Y., Chen, Q., Li, Y. J., Duan, J., Zhu, C.

1160   S., Dai, W. T., Wang, K., Lin, C. S., Ni, H. Y., Corbin, J. C., Wu, Y. F., Zhang, R. J., Tie,

1161   X. X., Hoffmann, T., O'Dowd, C., and Dusek, U.: Brown carbon aerosol in urban Xi'

1162   an, northwest China: the composition and light absorption properties, Environ. Sci.

1163   Technol., 52, 6825-6833, https://doi.org/10.1021/acs.est.8b02386, 2018.

1164   Huguet, A., Vacher, L., Relexans, S., Saubusse, S., Froidefond, J. M., and Parlanti,

1165   E.: Properties of fluorescent dissolved organic matter in the Gironde Estuary, Org.

1166   Geochem., 40, 706-719, https://doi.org/10.1016/j.orggeochem.2009.03.002, 2009.

1167   Jacobson, M. Z.: Isolating nitrated and aromatic aerosols and nitrated aromatic

1168   gases as sources of ultraviolet light absorption, J. Geophys. Res.: Atmos., 104, 3527-

3542, https://doi.org/10.1029/1998JD100054, 1999.

Jaoui, M., Corse, E., Kleindienst, T. E., Offenberg, J. H., Lewandowski, M., and Edney, E. O.: Analysis of secondary organic aerosol compounds from the photooxidation of d-limonene in the presence of NOX and their detection in ambient PM2.5, Environ. Sci. Technol., 40, 3819-3828, https://doi.org/10.1021/es052566z, 2006.

Jiang, W. Q., Misovich, M. V., Hettiyadura, A. P. S., Laskin, A., McFall, A. S., Anastasio, C., and Zhang, Q.: Photosensitized Reactions of a phenolic carbonyl from wood combustion in the aqueous phase—chemical evolution and light absorption properties of aqSOA, Environ. Sci. Technol., 55, 5199-5211, https://doi.org/10.1021/acs.est.0c07581, 2021.

Jiang, X. T., Liu, D. T., Li, Q., Tian, P., Wu, Y. Z., Li, S. Y., Hu, K., Ding, S., Bi, K., Li, R. J., Huang, M. Y., Ding, D. P., Chen, Q. C., Kong, S. F., Li, W. J., Pang, Y., and He, D.: Connecting the light absorption of atmospheric organic aerosols with oxidation state and polarity, Environ. Sci. Technol., 56, 12873-12885, https://doi.org/10.1021/acs.est.2c02202, 2022.

Jo, D. S., Park, R. J., Lee, S., Kim, S. W., and Zhang, X.: A global simulation of brown carbon: implications for photochemistry and direct radiative effect, Atmos. Chem. Phys., 16, 3413-3432, https://doi.org/10.5194/acp-16-3413-2016, 2016.

Kim, H. J., Collier, S., Ge, X. L., Xu, J. Z., Sun, Y. L., Jiang, W. Q., Wang, Y. L., Herckes, P., and Zhang, Q.: Chemical processing of water-soluble species and formation of secondary organic aerosol in fogs, Atmos. Environ., 200, 158-166, https://doi.org/10.1016/j.atmosenv.2018.11.062, 2019.

Kourtchev, I., O'Connor, I. P., Giorio, C., Fuller, S. J., Kristensen, K., Maenhaut, W., Wenger, J. C., Sodeau, J. R., Glasius, M., and Kalberer, M.: Effects of anthropogenic emissions on the molecular composition of urban organic aerosols: An ultrahigh resolution mass spectrometry study, Atmos. Environ., 89, 525-532, https://doi.org/10.1016/j.atmosenv.2014.02.051, 2014.

Kroll, J. H., Donahue, N. M., Jimenez, J. L., Kessler, S. H., Canagaratna, M. R., Wilson, K. R., Altieri, K. E., Mazzoleni, L. R., Wozniak, A. S., Bluhm, H., Mysak, E. R., Smith, J. D., Kolb, C. E., and Worsnop, D. R.: Carbon oxidation state as a metric

1199 for describing the chemistry of atmospheric organic aerosol, Nat. Chem., 3, 133-139,

1200 https://doi.org/10.1038/nchem.948, 2011.

1201 Kuang, Y., Shang, J., and Chen, Q. C.: Effect of ozone aging on light absorption

1202 and fluorescence of brown carbon in soot particles: The important role of polycyclic

1203 aromatic hydrocarbons, J. Hazard. Mater., 413, 125406,

1204 https://doi.org/10.1016/j.jhazmat.2021.125406, 2021.

1205 Kuang, Y., Shang, J., Sheng, M. S., Shi, X. D., Zhu, J. L., and Qiu, X. H.:

1206 Molecular Composition of Beijing PM(2.5) Brown Carbon Revealed by an Untargeted

1207 Approach Based on Gas Chromatography and Time-of-Flight Mass Spectrometry,

1208 Environ. Sci. Technol., 57, 909-919, https://doi.org/10.1021/acs.est.2c05918, 2023.

1209 Kumar, V., Giannoukos, S., Haslett, S. L., Tong, Y., Singh, A., Bertrand, A., Lee,

1210 C. P., Wang, D. S., Bhattu, D., Stefenelli, G., Dave, J. S., Puthussery, J. V., Qi, L., Vats,

1211 P., Rai, P., Casotto, R., Satish, R., Mishra, S., Pospisilova, V., Mohr, C., Bell, D. M.,

1212 Ganguly, D., Verma, V., Rastogi, N., Baltensperger, U., Tripathi, S. N., Prévôt, A. S. H.,

1213 and Slowik, J. G.: Highly time-resolved chemical speciation and source apportionment

1214 of organic aerosol components in Delhi, India, using extractive electrospray ionization

1215 mass spectrometry, Atmos. Chem. Phys., 22, 7739-7761, https://10.5194/acp-22-7739-

1216 2022, 2022.

1217 Laskin, A., Laskin, J., and Nizkorodov, S. A.: Chemistry of atmospheric brown

1218 carbon, Chem. Rev., 115, 4335-4382, https://doi.org/10.1021/cr5006167, 2015.

1219 Laskin, A., Smith, J. S., and Laskin, J.: Molecular characterization of nitrogen-

1220 containing organic compounds in biomass burning aerosols using high-resolution mass

1221 spectrometry, Environ. Sci. Technol., 43, 3764-3771,

1222 https://doi.org/10.1021/es803456n, 2009.

1223 Laskin, A., West, C. P., and Hettiyadura, A. P. S.: Molecular insights into the

1224 composition, sources, and aging of atmospheric brown carbon, Chem Soc Rev, 54,

1225 1583-1612, 10.1039/d3cs00609c, 2025.

1226 Lee, H. L., Laskin, A., Laskin, J., and Nizkorodov, S. A.: Excitation–emission

1227 spectra and fluorescence quantum yields for fresh and aged biogenic secondary organic

aerosols, Environ. Sci. Technol., 47, 5763-5770, https://doi.org/10.1021/es400644c, 2013.

Lei, R. Y., Sha, Y. Y., Meng, H. F., Huang, Y., Ye, J. H., Huang, D. D., Zhang, Y. J., Wu, Y., Li, Y. J., and Ge, X. L.: Aqueous phase photolysis of 4-nitrocatechol: Reaction kinetics, evolutions of chemical composition, light absorption and oxidation potential, Atmos. Environ., 343, 120981, https://doi.org/10.1016/j.atmosenv.2024.120981, 2025.

Li, H., Qin, X. F., Wang, G. C., Xu, J., Wang, Lu, D., Liu, C., Zheng, H., Liu, J. G., Huang, K., and Deng, C. R.: Conjoint impacts of continental outflows and marine sources on brown carbon in the East China sea: Abundances, optical properties, and formation processes, Atmos. Environ., 273, 118959, https://doi.org/10.1016/j.atmosenv.2022.118959, 2022a.

Li, H. W., Cui, L., Huang, Y., Zhang, Y. J., Wang, J. F., Chen, M. D., and Ge, X. L.: Concurrent dominant pathways of multifunctional products formed from nocturnal isoprene oxidation, Chemosphere, 322, 138185, https://doi.org/10.1016/j.chemosphere.2023.138185, 2023.

Li, M., Wang, X. F., Lu, C. Y., Li, R., Zhang, J., Dong, S. W., Yang, L. X., Xue, L., Chen, J. M., and Wang, W. X.: Nitrated phenols and the phenolic precursors in the atmosphere in urban Jinan, China, Sci. Total Environ., 714, 136760, https://doi.org/10.1016/j.scitotenv.2020.136760, 2020.

Li, M. J., Fan, X. J., Zhu, M. B., Zou, C. L., Song, J. Z., Wei, S. Y., Jia, W. L., and Peng, P. A.: Abundance and light absorption properties of brown carbon emitted from residential coal combustion in China, Environ. Sci. Technol., 53, 595-603, https://doi.org/10.1021/acs.est.8b05630, 2019.

Li, S., Chen, C., Yang, G.-l., Fang, J., Sun, Y., Tang, L., Wang, H., Xiang, W., Zhang, H., Croteau, P. L., Jayne, J. T., Liao, H., Ge, X., Favez, O., and Zhang, Y.: Sources and processes of organic aerosol in non-refractory PM1 and PM2.5 during foggy and haze episodes in an urban environment of the Yangtze River Delta, China, Environ. Res., 212, 113557, https://doi.org/10.1016/j.envres.2022.113557, 2022b.

Li, X. D., Tao, Y., Zhu, L. W., Ma, S. S., Luo, S. P., Zhao, Z. Z., Sun, N., Ge, X. L., and Ye, Z. L.: Optical and chemical properties and oxidative potential of aqueous-phase products from OH and 3C∗-initiated photooxidation of eugenol, Atmos. Chem. Phys., 22, 7793-7814, https://doi.org/10.5194/acp-22-7793-2022, 2022c.

Lin, G. X., Penner, J. E., Flanner, M. G., Sillman, S., Xu, L., and Zhou, C.: Radiative forcing of organic aerosol in the atmosphere and on snow: effects of SOA and brown carbon, J. Geophys. Res.: Atmos., 119, 7453-7476, https://doi.org/10.1002/2013JD021186, 2014.

Lin, P., Rincon, A. G., Kalberer, M., and Yu, J. Z.: Elemental composition of HULIS in the pearl river delta region, China: results inferred from positive and negative electrospray high resolution mass spectrometric data, Environ. Sci. Technol., 46, 7454-7462, https://doi.org/10.1021/es300285d, 2012.

Lin, P., Fleming, L. T., Nizkorodov, S. A., Laskin, J., and Laskin, A.: Comprehensive molecular characterization of atmospheric brown carbon by high resolution mass spectrometry with electrospray and atmospheric pressure photoionization, Anal. Chem., 90, 12493-12502, https://doi.org/10.1021/acs.analchem.8b02177, 2018.

Lin, P., Bluvshtein, N., Rudich, Y., Nizkorodov, S. A., Laskin, J., and Laskin, A.: Molecular chemistry of atmospheric brown carbon inferred from a nationwide biomass burning event, Environ. Sci. Technol., 51, 11561-11570, https://doi.org/10.1021/acs.est.7b02276, 2017.

Lin, P., Liu, J. M., Shilling, J. E., Kathmann, S. M., Laskin, J., and Laskin, A.: Molecular characterization of brown carbon (BrC) chromophores in secondary organic aerosol generated from photo-oxidation of toluene, Phys. Chem. Chem. Phys., 17, 23312-23325, https://doi.org/10.1039/C5CP02563J, 2015.

Lin, P., Aiona, P. K., Li, Y., Shiraiwa, M., Laskin, J., Nizkorodov, S. A., and Laskin, A.: Molecular characterization of brown carbon in ciomass curning aerosol particles, Environ. Sci. Technol., 50, 11815-11824, https://doi.org/10.1021/acs.est.6b03024, 2016.

Liu, S. J., Wang, Y. Q., Zhang, S., Chen, Y. B., Wu, C., Zhang, G. Q., and Wang, G. H.: The synergistic effect of NOx and SO2 on the formation and light absorption of secondary organic aerosols from o -xylene photooxidation, Atmos. Res., 304, https://doi.org/10.1016/j.atmosres.2024.107387, 2024.

Liu, Y., Li, H. W., Cui, S. J., Nie, D. Y., Chen, Y. F., and Ge, X. L.: Chemical Characteristics and Sources of Water-Soluble Organic Nitrogen Species in PM2.5 in Nanjing, China, https://doi.org/10.3390/atmos12050574, 2021.

Lobodin, V. V., Marshall, A. G., and Hsu, C. S.: Compositional space boundaries for organic compounds, Analytical Chemistry, 84, 3410-3416, https://doi.org/10.1021/ac300244f, 2012.

Ma, Y. L. and Hays, M. D.: Thermal extraction – two-dimensional gas chromatography–mass spectrometry with heart-cutting for nitrogen heterocyclics in biomass burning aerosols, J. Chromatogr. A, 1200, 228-234, https://doi.org/10.1016/j.chroma.2008.05.078, 2008.

Mao, J. F., Cheng, Y., Bai, Z., Zhang, W., Zhang, L. Y., Chen, H., Wang, L. N., Li, L., and Chen, J. M.: Molecular characterization of nitrogen-containing organic compounds in the winter North China Plain, Sci Total Environ, 838, 156189, https://10.1016/j.scitotenv.2022.156189, 2022.

Matos, J. T. V., Freire, S. M. S. C., Duarte, R. M. B. O., and Duarte, A. C.: Natural organic matter in urban aerosols: comparison between water and alkaline soluble components using excitation–emission matrix fluorescence spectroscopy and multiway data analysis, Atmos. Environ., 102, 1-10, https://doi.org/10.1016/j.atmosenv.2014.11.042, 2015.

McKnight, D. M., Boyer, E. W., Westerhoff, P. K., Doran, P. T., Kulbe, T., and Andersen, D. T.: Spectrofluorometric characterization of dissolved organic matter for indication of precursor organic material and aromaticity, Limnol. Oceanogr., 46, 38-48, https://doi.org/10.4319/lo.2001.46.1.0038, 2001.

McNeill, V. F.: Aqueous organic chemistry in the atmosphere: sources and

chemical processing of organic aerosols, Environ. Sci. Technol., 49, 1237-1244, https://doi.org/10.1021/es5043707, 2015.

Murphy, K. R., Stedmon, C. A., Graeber, D., and Bro, R.: Fluorescence spectroscopy and multi-way techniques. PARAFAC, Anal. Methods, 5, https://doi.org/10.1039/c3ay41160e, 2013.

Murphy, K. R., Hambly, A., Singh, S., Henderson, R. K., Baker, A., Stuetz, R., and Khan, S. J.: Organic matter fluorescence in municipal water recycling schemes: toward a unified PARAFAC model, Environ. Sci. Technol., 45, 2909-2916, https://doi.org/10.1021/es103015e, 2011.

Negron-Encarnacion, I. and Arce, R.: Light-induced transformations of aza-aromatic pollutants adsorbed on models of atmospheric particulate matter: Acridine and 9(10-H) acridone, Atmos. Environ., 41, 6771-6783, https://doi.org/10.1016/j.atmosenv.2007.04.062, 2007.

O'Brien, R. E., Ridley, K. J., Canagaratna, M. R., Jayne, J. T., Croteau, P. L., Worsnop, D. R., Budisulistiorini, S. H., Surratt, J. D., Follett, C. L., Repeta, D. J., and Kroll, J. H.: Ultrasonic nebulization for the elemental analysis of microgram-level samples with offline aerosol mass spectrometry, Atmos. Meas. Tech., 12, 1659-1671, https://doi.org/10.5194/amt-12-1659-2019, 2019.

Onasch, T. B., Trimborn, A., Fortner, E. C., Jayne, J. T., Kok, G. L., Williams, L. R., Davidovits, P., and Worsnop, D. R.: Soot particle aerosol mass spectrometer: development, validation, and initial application, Aerosol Sci. Technol., 46, 804-817, https://doi.org/10.1080/02786826.2012.663948, 2012.

Ou, Y., Nie, D. Y., Chen, H., Ye, Z. L., and Ge, X. L.: Characterization of products from the aqueous-phase photochemical oxidation of benzene-diols, Atmosphere, 12, https://doi.org/10.3390/atmos12050534, 2021.

Petters, S. S., Cui, T. Q., Zhang, Z. F., Gold, A., McNeill, V. F., Surratt, J. D., and Turpin, B. J.: Organosulfates from dark aqueous reactions of isoprene-derived epoxydiols under cloud and fog conditions: kinetics, mechanism, and effect of reaction environment on regioselectivity of sulfate addition, ACS Earth Space Chem., 5, 474-

486, https://doi.org/10.1021/acsearthspacechem.0c00293, 2021.

Powelson, M. H., Espelien, B. M., Hawkins, L. N., Galloway, M. M., and De Haan, D. O.: Brown Carbon Formation by Aqueous-Phase Carbonyl Compound Reactions with Amines and Ammonium Sulfate, Environ. Sci. Technol., 48, 985-993, https://doi.org/10.1021/es4038325, 2014.

Qi, L., Chen, M. D., Stefenelli, G., Pospisilova, V., Tong, Y. D., Bertrand, A., Hueglin, C., Ge, X. L., Baltensperger, U., Prévôt, A. S. H., and Slowik, J. G.: Organic aerosol source apportionment in Zurich using an extractive electrospray ionization time-of-flight mass spectrometer (EESI-TOF-MS) – Part 2: biomass burning influences in winter, Atmos. Chem. Phys., 19, 8037-8062, https://doi.org/10.5194/acp-19-8037-2019, 2019.

Qin, J. J., Zhang, L. M., Zhou, X. M., Duan, J. C., Mu, S. T., Xiao, K., Hu, J. N., and Tan, J. H.: Fluorescence fingerprinting properties for exploring water-soluble organic compounds in PM2.5 in an industrial city of northwest China, Atmos. Environ., 184, 203-211, https://doi.org/10.1016/j.atmosenv.2018.04.049, 2018.

Qin, Y. M., Tan, H. B., Li, Y. J., Schurman, M. I., Li, F., Canonaco, F., Prévôt, A. S. H., and Chan, C. K.: Impacts of traffic emissions on atmospheric particulate nitrate and organics at a downwind site on the periphery of Guangzhou, China, Atmos. Chem. Phys., 17, 10245-10258, https://doi.org/10.5194/acp-17-10245-2017, 2017.

Qiu, Y. M., Xie, Q. R., Wang, J. F., Xu, W. Q., Li, L. J., Wang, Q. Q., Zhao, J., Chen, Y. T., Chen, Y. F., Wu, Y. Z., Du, W., Zhou, W., Lee, J., Zhao, C. F., Ge, X. L., Fu, P. Q., Wang, Z., Worsnop, D. R., and Sun, Y. L.: Vertical characterization and source apportionment of water-soluble organic aerosol with high-resolution aerosol mass spectrometry in Beijing, China, ACS Earth Space Chem., 3, 273-284, https://doi.org/10.1021/acsearthspacechem.8b00155, 2019.

Shapiro, E. L., Szprengiel, J., Sareen, N., Jen, C. N., Giordano, M. R., and McNeill, V. F.: Light-absorbing secondary organic material formed by glyoxal in aqueous aerosol mimics, Atmos. Chem. Phys., 9, 2289-2300, https://doi.org/10.5194/acp-9-2289-2009,

2009.

Song, J. Z., Li, M. J., Fan, X. J., Zou, C. L., Zhu, M. B., Jiang, B., Yu, Z. Q., Jia, W. L., Liao, Y. H., and Peng, P. A.: Molecular Characterization of water- and methanol-soluble organic compounds emitted from residential coal combustion using ultrahigh-resolution electrospray ionization fourier transform ion cyclotron resonance mass spectrometry, Environ. Sci. Technol., 53, 13607-13617, https://doi.org/10.1021/acs.est.9b04331, 2019.

Stubbins, A., Lapierre, J. F., Berggren, M., Prairie, Y. T., Dittmar, T., and del Giorgio, P. A.: What's in an EEM? Molecular Signatures Associated with Dissolved Organic Fluorescence in Boreal Canada, Environ. Sci. Technol., 48, 10598-10606, https://doi.org/10.1021/es502086e, 2014.

Sun, Y. L., Du, W., Fu, P. Q., Wang, Q. Q., Li, J., Ge, X. L., Zhang, Q., Zhu, C. M., Ren, L. J., Xu, W. Q., Zhao, J., Han, T. T., Worsnop, D. R., and Wang, Z.: Primary and secondary aerosols in Beijing in winter: sources, variations and processes, Atmos. Chem. Phys., 16, 8309-8329, https://doi.org/10.5194/acp-16-8309-2016, 2016.

Tang, J., Li, J., Su, T., Han, Y., Mo, Y. Z., Jiang, H. X., Cui, M., Jiang, B., Chen, Y. J., Tang, J. H., Song, J. Z., Peng, P. A., and Zhang, G.: Molecular compositions and optical properties of dissolved brown carbon in biomass burning, coal combustion, and vehicle emission aerosols illuminated by excitation–emission matrix spectroscopy and Fourier transform ion cyclotron resonance mass spectrometry analysis, Atmos. Chem. Phys., 20, 2513-2532, https://doi.org/10.5194/acp-20-2513-2020, 2020.

Tang, J., Li, J., Zhao, S. Z., Zhong, G. C., Mo, Y. Z., Jiang, H. X., Jiang, B., Chen, Y. J., Tang, J. H., Tian, C. G., Zong, Z., Hussain S., J., Song, J. Z., and Zhang, G.: Molecular signatures and formation mechanisms of water-soluble chromophores in particulate matter from Karachi in Pakistan, Sci. Total Environ., 914, 169890, https://doi.org/10.1016/j.scitotenv.2024.169890, 2024.

Tsugawa, H., Cajka, T., Kind, T., Ma, Y., Higgins, B., Ikeda, K., Kanazawa, M., VanderGheynst, J., Fiehn, O., and Arita, M.: MS-DIAL: data-independent MS/MS deconvolution for comprehensive metabolome analysis, Nat. Methods, 12, 523-526,

https://doi.org/10.1038/nmeth.3393, 2015.

Ulbrich, I. M., Canagaratna, M. R., Zhang, Q., Worsnop, D. R., and Jimenez, J. L.: Interpretation of organic components from Positive Matrix Factorization of aerosol mass spectrometric data, Atmos. Chem. Phys., 9, 2891-2918, https://doi.org/10.5194/acp-9-2891-2009, 2009.

Updyke, K. M., Nguyen, T. B., and Nizkorodov, S. A.: Formation of brown carbon via reactions of ammonia with secondary organic aerosols from biogenic and anthropogenic precursors, Atmos. Environ., 63, 22-31, https://doi.org/10.1016/j.atmosenv.2012.09.012, 2012.

Vasilakopoulou, C. N., Florou, K., Kaltsonoudis, C., Stavroulas, I., Mihalopoulos, N., and Pandis, S. N.: Development and evaluation of an improved offline aerosol mass spectrometry technique, Atmos. Meas. Tech., 16, 2837-2850, https://doi.org/10.5194/amt-16-2837-2023, 2023.

Veld, M., Khare, P., Hao, Y. F., Reche, C., Pérez, N., Alastuey, A., Yus-Díez, J., Marchand, N., Prevot, A. S. H., Querol, X., and Daellenbach, K. R.: Characterizing the sources of ambient PM10 organic aerosol in urban and rural Catalonia, Spain, Sci. Total Environ., 902, 166440, https://doi.org/10.1016/j.scitotenv.2023.166440, 2023.

Wang, D. W., Shen, Z. X., Zhang, Q., Lei, Y. L., Zhang, T., Huang, S. S., Sun, J., Xu, H. M., and Cao, J. J.: Winter brown carbon over six of China's megacities: light absorption, molecular characterization, and improved source apportionment revealed by multilayer perceptron neural network, Atmos. Chem. Phys., 22, 14893-14904, https://doi.org/10.5194/acp-22-14893-2022, 2022a.

Wang, J. F., Ge, X. L., Sonya, C., Ye, J. H., Lei, Y. L., Chen, M. D., and Zhang, Q.: Influence of regional emission controls on the chemical composition, sources, and size distributions of submicron aerosols: Insights from the 2014 Nanjing Youth Olympic Games, Sci. Total Environ., 807, 150869, https://doi.org/10.1016/j.scitotenv.2021.150869, 2022b.

Wang, J. F., Ge, X. L., Chen, Y. F., Shen, Y. F., Zhang, Q., Sun, Y. L., Xu, J. Z., Ge, S., Yu, H., and Chen, M. D.: Highly time-resolved urban aerosol characteristics during

springtime in Yangtze River Delta, China: insights from soot particle aerosol mass spectrometry, Atmos. Chem. Phys., 16, 9109-9127, https://doi.org/10.5194/acp-16-9109-2016, 2016.

Wang, J. F., Ye, J. H., Zhang, Q., Zhao, J., Wu, Y. Z., Li, J. Y., Liu, D. T., Li, W. J., Zhang, Y. G., Wu, C., Xie, C. H., Qin, Y. M., Lei, Y. L., Huang, X. P., Guo, J. P., Liu, P. F., Fu, P. Q., Li, Y. J., Lee, H. C., Choi, H., Zhang, J., Liao, H., Chen, M. D., Sun, Y. L., Ge, X. L., Martin, S. T., and Jacob, D. J.: Aqueous production of secondary organic aerosol from fossil-fuel emissions in winter Beijing haze, Proc. Natl. Acad. Sci. U. S. A., 118, https://doi.org/10.1073/pnas.2022179118, 2021.

Wang, K., Zhang, Y., Huang, R. J., Cao, J. J., and Hoffmann, T.: UHPLC-Orbitrap mass spectrometric characterization of organic aerosol from a central European city (Mainz, Germany) and a Chinese megacity (Beijing), Atmos. Environ., 189, 22-29, https://doi.org/10.1016/j.atmosenv.2018.06.036, 2018a.

Wang, L. W., Wang, X. F., Gu, R. R., Wang, H., Yao, L., Wen, L., Zhu, F. P., Wang, W. H., Xue, L. K., Yang, L. X., Lu, K. D., Chen, J. M., Wang, T., Zhang, Y. H., and Wang, W. X.: Observations of fine particulate nitrated phenols in four sites in northern China: concentrations, source apportionment, and secondary formation, Atmos. Chem. Phys., 18, 4349-4359, https://doi.org/10.5194/acp-18-4349-2018, 2018b.

Wang, Y., Huang, R. J., Zhong, H. B., Wang, T., Yang, L., Yuan, W., Xu, W., and An, Z. S.: Predictions of the Optical Properties of Brown Carbon Aerosol by Machine Learning with Typical Chromophores, Environ. Sci. Technol., 58, 20588-20597, https://doi.org/10.1021/acs.est.4c09031, 2024.

Wang, Y. J., Hu, M., Lin, P., Guo, Q. F., Wu, Z. J., Li, M. G., Zeng, L. M., Song, Y., Zeng, L. W., Wu, Y. S., Guo, S., Huang, X. F., and He, L. Y.: Molecular characterization of nitrogen-containing organic compounds in humic-like substances emitted from straw residue burning, Environ. Sci. Technol., 51, 5951-5961, https://doi.org/10.1021/acs.est.7b00248, 2017.

Wang, Y. Q.: An open source software suite for multi-dimensional meteorological data computation and visualisation, Journal of Open Research Software, 7,

https://doi.org/10.5334/jors.267, 2019.

Wen, H., Zhou, Y., Xu, X. Y., Wang, T. S., Chen, Q. L., Chen, Q. C., Li, W. J., Wang, Z., Huang, Z. W., Zhou, T., Shi, J. S., Bi, J. R., Ji, M. X., and Wang, X.: Water-soluble brown carbon in atmospheric aerosols along the transport pathway of Asian dust: Optical properties, chemical compositions, and potential sources, Sci. Total Environ., 789, 147971, https://doi.org/10.1016/j.scitotenv.2021.147971, 2021.

Wu, G. M., Ram, K., Fu, P. Q., Wang, W., Zhang, Y. L., Liu, X. Y., Stone, E. A., Pradhan, B. B., Dangol, P. M., Panday, A. K., Wan, X., Bai, Z. P., Kang, S. C., Zhang, Q. G., and Cong, Z. Y.: Water-soluble brown carbon in atmospheric aerosols from Godavari (Nepal), a regional representative of south Asia, Environ. Sci. Technol., 53, 3471-3479, https://doi.org/10.1021/acs.est.9b00596, 2019a.

Wu, Y. Z., Ge, X. L., Wang, J. F., Shen, Y. F., Ye, Z. L., Ge, S., Wu, Y., Yu, H., and Chen, M. D.: Responses of secondary aerosols to relative humidity and photochemical activities in an industrialized environment during late winter, Atmos. Environ., 193, 66-78, https://doi.org/10.1016/j.atmosenv.2018.09.008, 2018.

Wu, Y. Z., Liu, D. T., Wang, J. F., Shen, F. Z., Chen, Y. F., Cui, S. J., Ge, S., Wu, Y., Chen, M. D., and Ge, X. L.: Characterization of size-resolved hygroscopicity of black carbon-containing particle in urban environment, Environ. Sci. Technol., 53, 14212-14221, https://doi.org/10.1021/acs.est.9b05546, 2019b.

Xian, J. K., Cui, S. J., Chen, X. Z., Wang, J. Y., Xiong, Y. F., Gu, C. J., Wang, Y., Zhang, Y. J., Li, H. W., Wang, J. F., and Ge, X. L.: Online chemical characterization of atmospheric fine secondary aerosols and organic nitrates in summer Nanjing, China, Atmos. Res., 290, 106783, https://doi.org/10.1016/j.atmosres.2023.106783, 2023.

Xie, M. J., Mladenov, N., Williams, M. W., Neff, J. C., Wasswa, J., and Hannigan, M. P.: Water soluble organic aerosols in the Colorado Rocky Mountains, USA: composition, sources and optical properties, Sci. Rep., 6, 39339, https://doi.org/10.1038/srep39339, 2016.

Xie, X. C., Chen, Y. F., Nie, D. Y., Liu, Y., Liu, Y., Lei, R. Y., Zhao, X. Y., Li, H. W., and Ge, X. L.: Light-absorbing and fluorescent properties of atmospheric brown

carbon: A case study in Nanjing, China, Chemosphere, 251, 126350, https://doi.org/10.1016/j.chemosphere.2020.126350, 2020.

Xing, C., Wan, Y. B., Wang, Q. Q., Kong, S. F., Huang, X. P., Ge, X. L., Xie, M. J., and Yu, H.: Molecular Characterization of Brown Carbon Chromophores in Atmospherically Relevant Samples and Their Gas-Particle Distribution and Diurnal Variation in the Atmosphere, J. Geophys. Res.: Atmos., 128, e2022JD038142, https://doi.org/10.1029/2022JD038142, 2023.

Xu, L. L., Lin, G. X., Liu, X. H., Wu, C. L., Wu, Y. F., and Lou, S. J.: Constraining Light Absorption of Brown Carbon in China and Implications for Aerosol Direct Radiative Effect, Geophys. Res. Lett., 51, https://doi.org/10.1029/2024gl109861, 2024.

Yan, G. and Kim, G.: Speciation and sources of brown carbon in precipitation at seoul, Korea: insights from excitation−emission matrix spectroscopy and carbon isotopic analysis, Environ. Sci. Technol., 51, 11580-11587, https://doi.org/10.1021/acs.est.7b02892, 2017.

Yan, J. P., Wang, X. P., Gong, P., Wang, C. F., and Cong, Z. Y.: Review of brown carbon aerosols: recent progress and perspectives, Sci. Total Environ., 634, 1475-1485, https://doi.org/10.1016/j.scitotenv.2018.04.083, 2018.

Yassine, M. M., Harir, M., Dabek-Z., E., and Schmitt-K., P.: Structural characterization of organic aerosol using Fourier transform ion cyclotron resonance mass spectrometry: Aromaticity equivalent approach, Rapid Commun. Mass Spectrom., 28, 2445-2454, https://doi.org/doi.org/10.1002/rcm.7038, 2014.

Ye, Z. L., Qu, Z. X., Ma, S. S., Luo, S. P., Chen, Y. T., Chen, H., Chen, Y. F., Zhao, Z. Z., Chen, M. D., and Ge, X. L.: A comprehensive investigation of aqueous-phase photochemical oxidation of 4-ethylphenol, Sci. Total Environ., 685, 976-985, https://doi.org/10.1016/j.scitotenv.2019.06.276, 2019.

Ye, Z. L., Li, Q., Liu, J. S., Luo, S. P., Zhou, Q. F., Bi, C. L., Ma, S. S., Chen, Y. F., Chen, H., Li, L., and Ge, X. L.: Investigation of submicron aerosol characteristics in Changzhou, China: Composition, source, and comparison with co-collected PM2.5, Chemosphere, 183, 176-185, https://doi.org/10.1016/j.chemosphere.2017.05.094, 2017.

Yu, H. R., Liang, H., Qu, F. S., Han, Z. S., Shao, S. L., Chang, H. Q., and Li, G. B.: Impact of dataset diversity on accuracy and sensitivity of parallel factor analysis model of dissolved organic matter fluorescence excitation-emission matrix, Sci. Rep., 5, 10207, https://doi.org/10.1038/srep10207, 2015.

Yu, J. T., Yan, C. Q., Liu, Y., Li, X. Y., Zhou, T., and Zheng, M.: Potassium: a tracer for biomass burning in Beijing?, Aerosol Air Qual. Res., 18, 2447-2459, https://doi.org/10.4209/aaqr.2017.11.0536, 2018.

Zhang, B. Q., Zhang, Y. J., Zhang, K. X., Zhang, Y. C., Ji, Y., Zhu, B. Z., Liang, Z. Y., Wang, H. L., and Ge, X. L.: Machine learning assesses drivers of PM2.5 air pollution trend in the Tibetan Plateau from 2015 to 2022, Sci. Total Environ., 878, 163189, https://doi.org/10.1016/j.scitotenv.2023.163189, 2023.

Zhang, Q., Jimenez, J. L., Canagaratna, M. R., Ulbrich, I. M., Ng, N. L., Worsnop, D. s. R., and Sun, Y. L.: Understanding atmospheric organic aerosols via factor analysis of aerosol mass spectrometry: a review, Anal. Bioanal. Chem., 401, 3045-3067, https://doi.org/10.1007/s00216-011-5355-y, 2011.

Zhang, S. Y.: Detection of scopolamine in nori fruit juice and its traditional chinese medicine compound health products by high performance liquid chromatography, World Latest Medicine Information, 18, 91-92, https://doi.org/10.19613/j.cnki.1671-3141.2018.82.066, 2018.

Zhang, X. L., Lin, Y. H., Surratt, J. D., and Weber, R. J.: Sources, composition and absorption Ångström exponent of light-absorbing organic components in aerosol extracts from the Los Angeles basin, Environ. Sci. Technol., 47, 3685-3693, https://doi.org/10.1021/es305047b, 2013.

Zhang, Y. Z., Forrister, H., Liu, J. M., Dibb, J., Anderson, B., Schwarz, J. P., Perring, A. E., Jimenez, J. L., Campuzano-Jost, P., Wang, Y. H., Nenes, A., and Weber, R. J.: Top-of-atmosphere radiative forcing affected by brown carbon in the upper troposphere, Nat. Geosci., 10, 486-489, https://doi.org/10.1038/ngeo2960, 2017.

Zhao, R., Lee, A. K. Y., Huang, L., Li, X., Yang, F., and Abbatt, J. P. D.: Photochemical processing of aqueous atmospheric brown carbon, Atmos. Chem. Phys.,

15, 6087-6100, https://doi.org/10.5194/acp-15-6087-2015, 2015.

Zhong, M., Xu, J. Z., Wang, H. Q., Gao, L., Zhu, H. X., Zhai, L. X., Zhang, X. H., and Zhao, W. H.: Characterizing water-soluble brown carbon in fine particles in four typical cities in northwestern China during wintertime: integrating optical properties with chemical processes, Atmos. Chem. Phys., 23, 12609-12630, https://doi.org/10.5194/acp-23-12609-2023, 2023.

Zhu, B., Fang, J., Zhang, Y., Qiu, J., Chen, K., Zhang, K., Liang, H., Yang, H., Ding, Y., and Ge, X.: Machine learning elucidates ubiquity of enhanced ozone air pollution in China linked to the spring festival effect, Atmos. Pollut. Res., 15, 102127, https://doi.org/10.1016/j.apr.2024.102127, 2024.

Zhu, J. J., Yang, M., and Ren, Z. J.: Machine Learning in Environmental Research: Common Pitfalls and Best Practices, Environ Sci Technol, 57, 17671-17689, https://doi.org/10.1021/acs.est.3c00026, 2023.

Zorn, S. R., Drewnick, F., Schott, M., Hoffmann, T., and Borrmann, S.: Characterization of the South Atlantic marine boundary layer aerosol using an aerodyne aerosol mass spectrometer, Atmos. Chem. Phys., 8, 4711-4728, https://doi.org/10.5194/acp-8-4711-2008, 2008.

Zsolnay, A., Baigar, E., Jimenez, M., Steinweg, B., and Saccomandi, F.: Differentiating with fluorescence spectroscopy the sources of dissolved organic matter in soils subjected to drying, Chemosphere, 38, 45-50, https://doi.org/10.1016/S0045-6535(98)00166-0, 1999.

1567   Table 1. The average mass concentrations of major chemical components as well as the

1568   parameters of optical properties of PM$_{2.5}$ collected in Nanjing during two seasons.

	Summer Season (SS)			Cold Season (CS)		
	Daytime	Nighttime	Average	Daytime	Nighttime	Average
OC (μg m^{-3})	7.02±3.04	6.87±2.51	6.94±2.76	12.9±5.77	12.74±5.29	12.82±5.51
EC (μg m^{-3})	1.13±0.31	1.22±0.37	1.17±0.34	1.94±0.93	1.6±0.74	1.77±0.86
AAE$_{WSOC}$	6.34±0.65	6.35±0.69	6.35±0.67	6.43±0.68	6.44±0.86	6.43±0.77
AAE$_{MSOC}$	6.02±0.90	5.96±0.96	5.99±0.92	7.06±0.94	6.70±0.65	6.89±0.82
WSOC (μg m^{-3})	4.06±1.31	4.45±1.44	4.26±1.38	5.81±2.29	5.75±2.25	6.34±2.27
MSOC (μg m^{-3})	5.64±2.12	5.79±1.89	5.72±1.99	10.42±4.98	10.49±4.57	10.45±4.75
Total ions (μg m^{-3})	18.00±5.49	18.69±8.05	18.49±6.91	35.41±15.02	43.12±17.94	39.22±16.88
Abs$_{365, WSOC}$ (M m^{-1})	2.15±0.90	2.38±0.80	2.27±0.85	4.89±2.63	4.86±2.46	4.87±2.53
Abs$_{365, MSOC}$ (M m^{-1})	3.44±1.40	3.82±1.55	3.64±1.48	4.65±2.24	5.31±2.71	4.97±2.49
MAE$_{365, WSOC}$ (m^2 g^{-1})	0.54±0.16	0.56±0.15	0.55±0.16	0.73±0.20	0.77±0.21	0.75±0.21
MAE$_{365, MSOC}$ (m^2 g^{-1})	0.68±0.32	0.75±0.30	0.72±0.31	0.48±0.18	0.52±0.16	0.50±0.17
SFE$_{WSOC}$(W g^{-1})	2.16±1.29	2.24±1.36	2.20±1.33	3.16±1.8	3.42±1.25	3.24±1.84
SFE$_{MSOC}$(W g^{-1})	2.28±2.37	2.55±1.85	2.43±2.10	2.19±1.01	2.26±0.81	2.23±0.91

1569

1570 Table 2. Multi-linear regression results of the four factors and corresponding average

1571 contributions to the total light absorption of water-soluble organics (WSOA).

Factor	Regression Coefficient($m^2 \cdot g^{-1}$)		Contribution (%)
	Average	Standard Error	
HOA	0.71	0.11	33.05
BBOA	0.71	0.06	15.49
OOA1	0.12	0.07	6.00
OOA2	0.83	0.14	45.46

1572

1573   Table 3. The average values of fluorescence indices of both water-soluble organic

1574   carbon (WSOC) and methanol-soluble organic carbon (MSOC).

	Summer Season (SS)			Cold Season (CS)		
	Day	Night	Average	Day	Night	Average
HIX_{WSOC}	3.16±0.74	3.51±1.12	3.34±0.97	4.68±0.94	4.67±0.91	4.68±0.92
HIX_{MSOC}	2.65±0.99	2.78±0.86	2.72±0.92	3.42±0.73	3.53±0.58	3.48±0.66
FI_{WSOC}	1.85±0.16	1.97±0.17	1.91±0.18	1.89±0.11	1.92±0.09	1.90±0.10
FI_{MSOC}	2.25±0.26	2.30±0.31	2.27±0.28	2.10±0.15	2.12±0.14	2.11±0.15
BIX_{WSOC}	0.81±0.16	0.86±0.14	0.84±0.15	0.86±0.10	0.91±0.08	0.88±0.09
BIX_{MSOC}	0.89±0.19	0.9±0.13	0.90±0.16	0.95±0.10	0.97±0.11	0.96±0.10

1575

1576   Table 4. The number percentages of organosulfates (OSs) in CHOS compounds in ESI⁻

1577   mode and those of nitrooxy-OSs in CHONS compounds in both modes.

	SS		CS	
	Daytime	Nighttime	Daytime	Nighttime
OSs (ESI⁻)	34.8%	42.3%	54.3%	68.6%
Nitrooxy-OSs (ESI⁻)	5.3%	12.0%	11.0%	12.5%
Nitrooxy-OSs (ESI⁺)	10.3%	11.8%	10.5%	9.8%

1578

1579
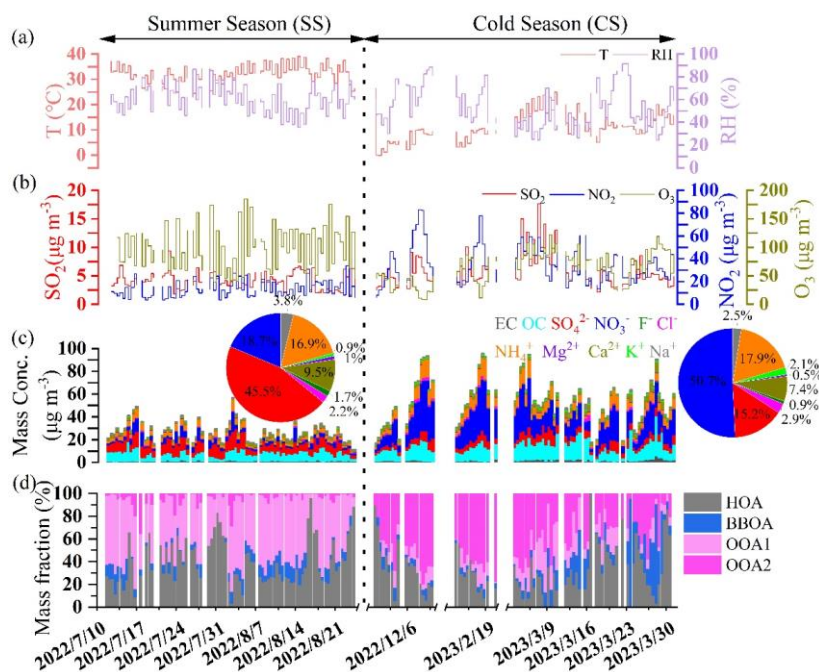
1580

Figure 1. Time series of: (a) air temperature (T) and relative humidity (RH); (b) concentrations of nitrogen dioxide (NO₂), sulfur dioxide (SO₂) and ozone (O₃); (c) concentrations of different inorganic ions, total organic carbon (OC), and elemental carbon (EC) (two inset pies are the average mass contributions of difference ions to the total ions during SS and CS, respectively); and (d) mass percentages of different factors with respect to the total water-soluble OA

1587
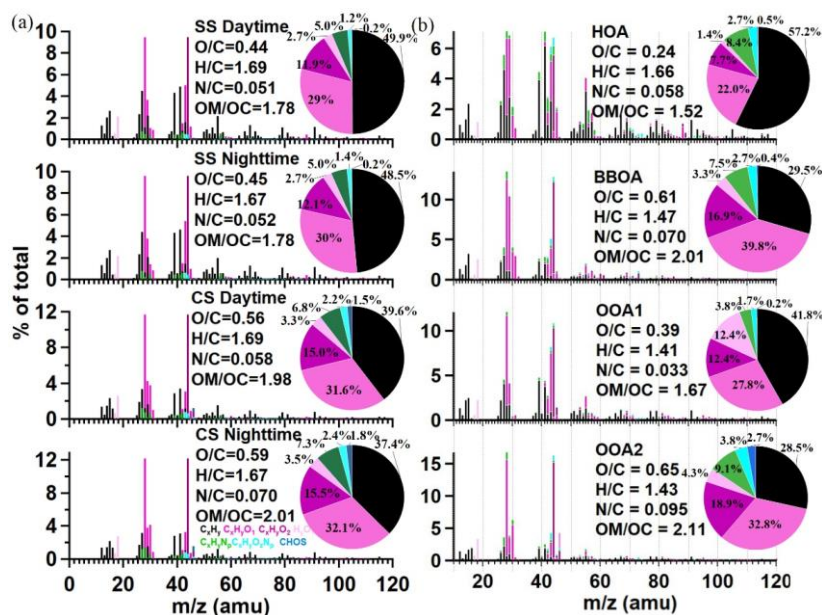
1588

1589   Figure 2. High-resolution mass spectra (HRMS) of (a) the water-soluble OA (WSOA)

1590   during different periods, and (b) the four resolved factors (HOA, BBOA, OOA1,

1591   OOA2). Ions are classified into and colored by different ion families, and inset pies in

1592   both charts show the mass fractional contributions of different ion families to the total

1593   HRMS correspondingly.

1594
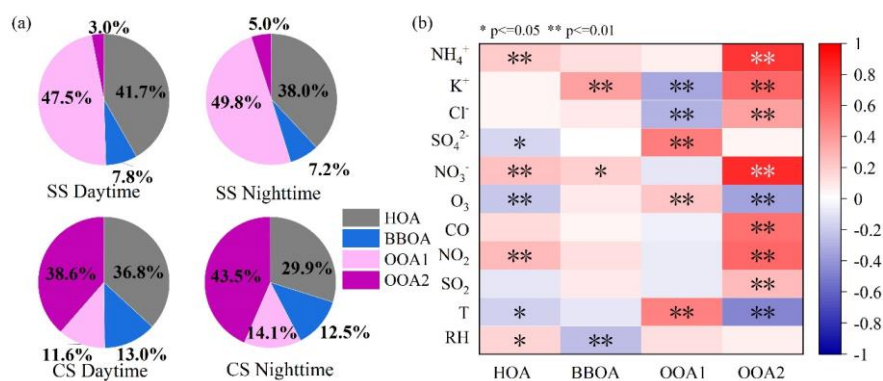
Figure 3. (a) Average mass contributions of the four factor to WSOA during different periods, and (b) cross-correlation coefficients (Pearson's *r*) among the four factors and other aerosol components as well as gaseous species.

1600
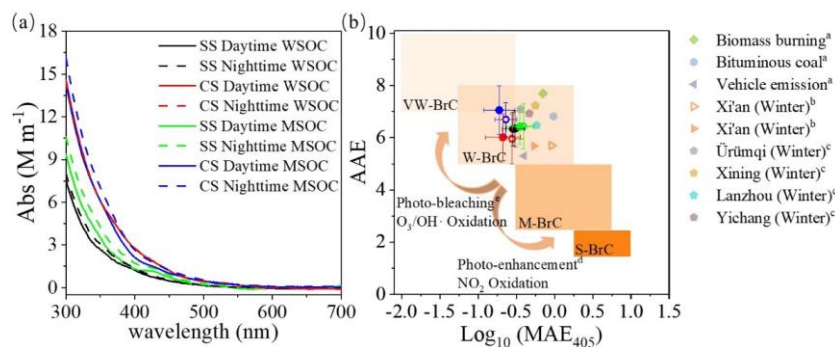
1601 Figure 4. (a) Light absorption coefficients (Abs) of the water-soluble OC (WSOC) and

1602 methanol-soluble OC (MSOC) as a function of wavelength, and (b) distribution of the

1603 measured data in the $log_{10}(MAE_{405})$-AAE space (Saleh, 2020)(MAE_{405}: Mass

1604 absorption efficiency at 405 nm; AAE: Absorption Ångström Exponent; The shaded

1605 areas indicate very weakly (VW), weakly (W), moderately (M), and strongly (S)

1606 absorbing brown carbon (BrC), respectively; Other markers indicate results from [a]

1607 Huang et al. (2018), [b] Chen et al. (2018) and [c] Zhong et al. (2023).

1608

1609
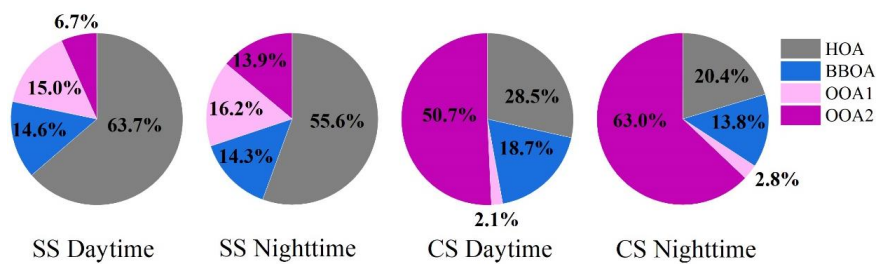
1610   Figure 5. Contributions of the four factors to the total light absorption of WSOA during

1611   different periods.
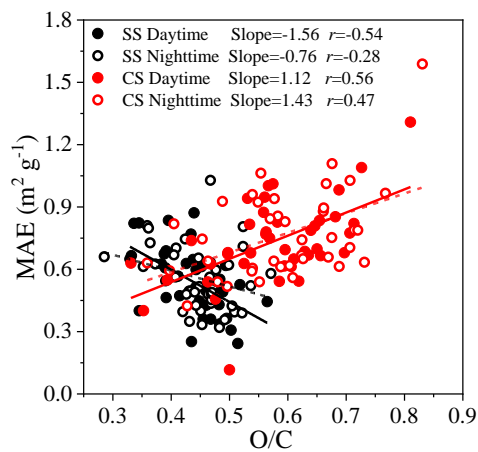
1612

1613   Figure 6. Scatter plot of MAE$_{365}$ (mass absorption efficiency at 365 nm) versus the

1614   oxygen-to-carbon (O/C) ratios for the WSOA.
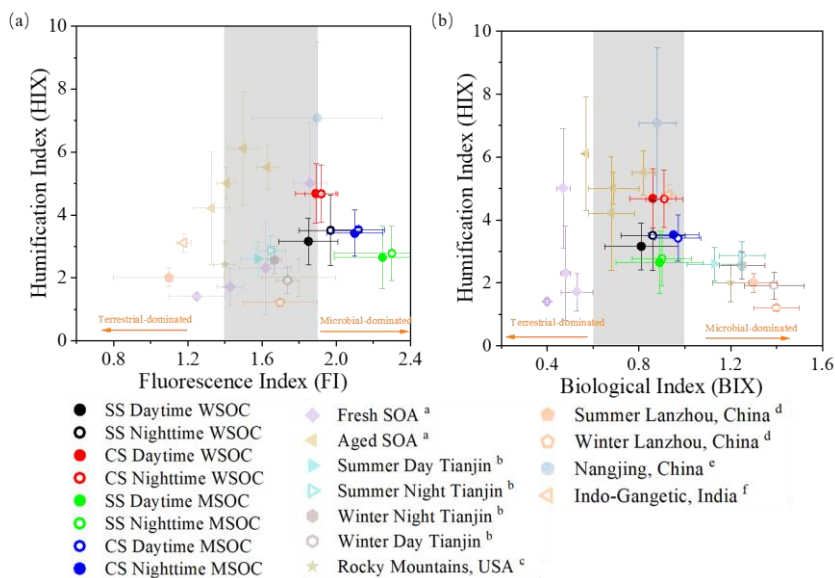
1615

1616 Figure 7. Distribution of the fluorescent indices of measured data in this study and a

1617 few other studies ([a] Lee et al. (2013), [b] Deng et al. (2022), [c] Xie et al. (2016), [d] Qin et

1618 al. (2018), [e] Xie et al. (2016), [f] Dey et al. (2021)): (a) Humidication index (HIX) versus

1619 fluorescenc index (FI), and (b) HIX versus biological index (BIX). The shaded areas

1620 marked 0.6 ~ 1 of BIX (Huguet et al., 2009) and 1.6 ~ 1.9 of FI (Mcknight et al., 2001).

1621
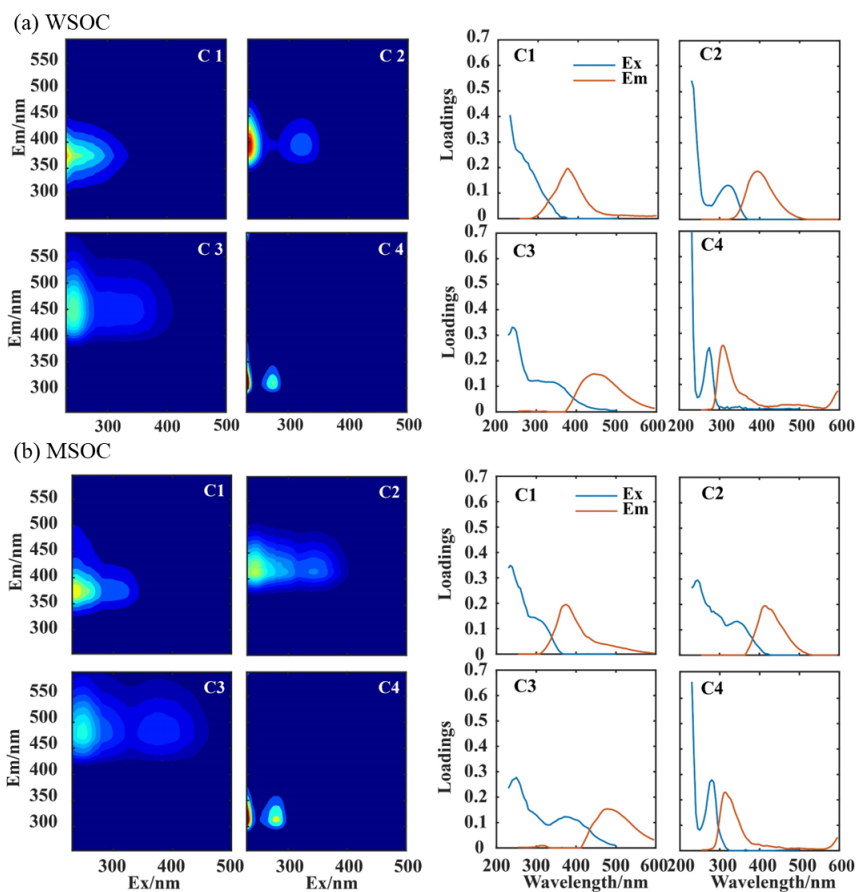
Figure 8. Four fluorescence components (C1 ~ C4) and the corresponding fluorescent intensities of emission (brown) and excitation (blue) against wavelenghth: (a) WSOC, and (b) MSOC.
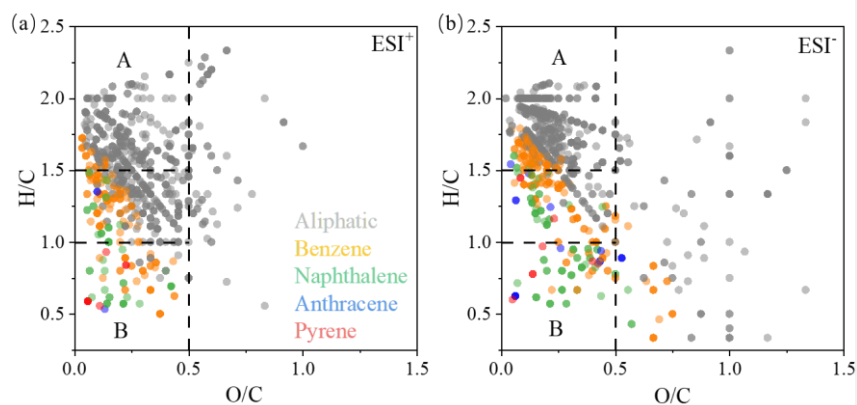
1628
1629
1630   Figure 9. Van Krevelen diagram for CHO compounds detected in (a) ESI⁺ and (b) ESI⁻

1631   mode. The markers with different colors represent aliphatic compounds ($Xc < 2.50$),

1632   aromatic benzene ring structures ($2.50 \leq Xc < 2.71$), naphthalene ring structures (2.71

1633 $\leq Xc < 2.80$), anthracene ring structures ($2.80 \leq Xc < 2.83$), and pyrene ring structures

1634   ($2.83 \leq Xc < 2.92$), respectively (Mao et al., 2022).

1635
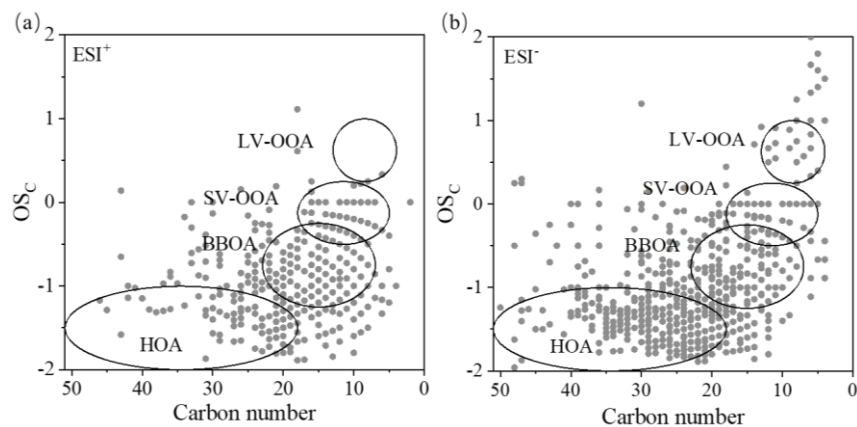
1636

1637 Figure 10. Scatter plots of carbon oxidation state (OSc) versus carbon number for CHO

1638 compounds: (a) ESI⁺ mode, and (b) ESI⁻ mode. The circled areas represent those from

1639 fossil fuel combustion hydrocarbon-like OA (HOA), biomass burning OA (BBOA),

1640 semi-volatile oxygenated OA (SV-OOA) and low-volatility oxygenated OA (LV-

1641 OOA)(Kroll et al., 2011).

1642
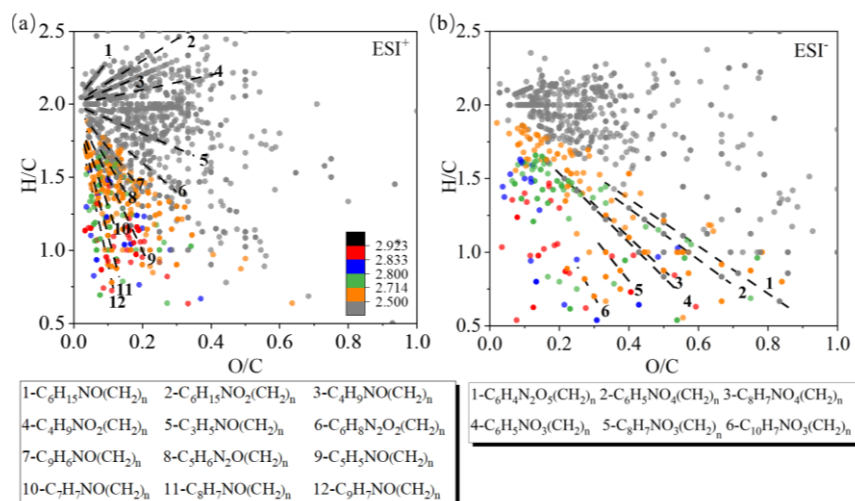
1645   Figure 11. Van Krevelen diagram for CHON compounds detected in both ESI$^+$ and ESI$^-$

1646   mode. The data are also colored by Xc values (See caption of Fig. 9), and the different

1647   dash lines represent different series of compounds.

1648

1649
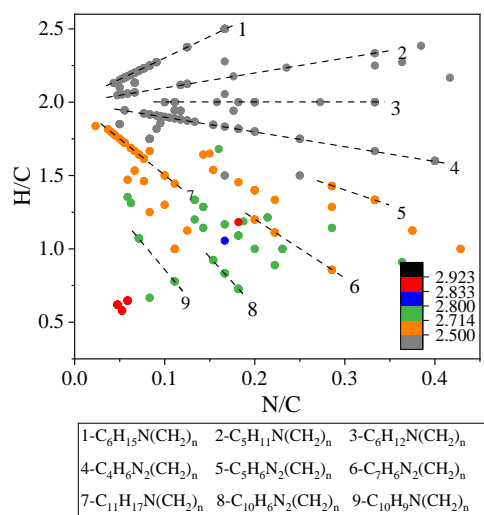
1650

1651

1652 Figure 12. Van Krevelen diagram of the CHN compounds in ESI$^+$ mode. The data are

1653 also colored by Xc values (See caption of Fig. 9), and the different dash lines represent

1654 different series of compounds.

1655

1656
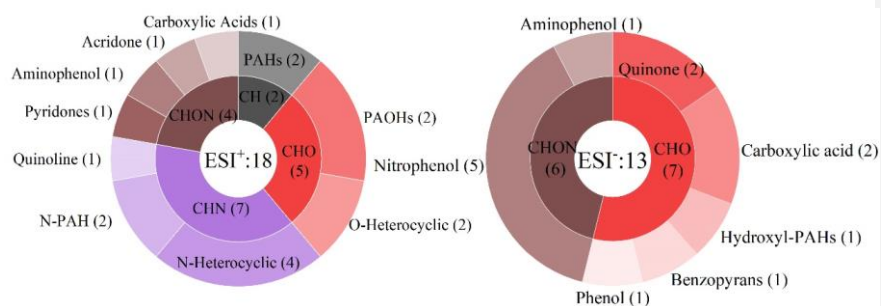
1657 Figure 13. Distributions of the machine learning identified key light absorbing organic

1658 compounds (details in Table S2 in the supplement)

1659